Journal of
Nuclear Engineering

MDPI

Article

Best Practices for Axial Flow-Induced Vibration (FIV) Simulation in Nuclear Applications

Anas Muhamad Pauzi [1,*], Wenyu Mao [2,3], Andrea Cioncolini [4], Eddie Blanco-Davis [5] and Hector Iacovides [1]

[1] School of Engineering, The University of Manchester, Manchester M13 9PL, UK; h.iacovides@manchester.ac.uk
[2] Shanghai Nuclear Engineering Research and Design Institute, Shanghai 200233, China; maowenyu@snerdi.com.cn or maowenyu@sjtu.edu.cn
[3] School of Mechanical Engineering, Shanghai Jiao Tong University, Shanghai 200240, China
[4] Department of Mechanical Engineering (Robotics), Guangdong Technion-Israel Institute of Technology (GTIIT), Shantou 515063, China; andrea.cioncolini@gtiit.edu.cn
[5] Liverpool Logistics, Offshore and Marine Research Institute (LOOM), Liverpool John Moores University, Liverpool L3 3AF, UK; e.e.blancodavis@ljmu.ac.uk
* Correspondence: anasmpauzi@gmail.com

Abstract

Fretting wear due to flow-induced vibration (FIV) remains a primary cause of fuel failure in light water nuclear reactors. In the study of axial FIV, i.e., FIV caused by axial flows, three vibration characteristics, namely natural frequency, damping ratio, and root-mean-square (RMS) amplitude, are critical for mitigating fretting wear by avoiding resonance, maximising overdamping, and preventing large-amplitude instability motion, respectively. This paper presents a set of best practices for simulating axial FIV with a focus on predicting these parameters based on a URANS-FSI numerical framework, utilising high-Reynolds-number Unsteady Reynolds-Averaged Navier–Stokes (URANS) turbulence modelling and two-way fluid–structure interaction (FSI) coupling. This strategy enables accurate and efficient prediction of vibration parameters and offers promising scalability for full-scale nuclear fuel assembly applications. Validation is performed against a semi-empirical model to predict RMS amplitude and experimental benchmarking. The validation experiments involve two setups: vibration of a square beam with fixed and roller-supported ends in annular flow tested at Vattenfall AB, and self-excited vibration of a cantilever beam in annular flow tested at the University of Manchester. The study recommends best practices for numerical schemes, mesh strategies, and convergence criteria, tailored to improve the accuracy and efficiency for each validated parameter.

Keywords: fluid–structure interaction (FSI); computational fluid dynamics (CFD); nuclear fuel rods; fretting wear; Foam-Extend; solids4Foam; OpenFOAM

Academic Editor: Dan Gabriel Cacuci

Received: 1 July 2025
Revised: 5 December 2025
Accepted: 19 December 2025
Published: 25 December 2025

1. Introduction

Flow-induced vibrations (FIVs) remain a significant challenge in water-cooled nuclear reactors due to their potential to cause grid-to-rod fretting (GTRF), a leading cause of fuel rod failure. GTRF was responsible for approximately 75% of fuel failures in light water reactors between 1999 and 2002 [1]. Although improvements in fuel design, such as heat-treated springs and enhanced cladding, reduced this figure to 57% between 2006 and 2015 [2], GTRF remains a persistent issue.

Notably, even advanced reactors such as the European Pressurised Reactor (EPR) in Taishan, China, experienced extended shutdowns due to GTRF in 2021 [3,4]. This highlights

the limitations of current predictive capabilities and the need for more accurate numerical tools. Validated computational fluid dynamics and fluid–structure interaction (CFD-FSI) simulations are essential at the design stage to reduce FIV susceptibility and enhance fuel reliability. Such challenges have motivated ongoing efforts to develop robust simulation methodologies under industrial conditions.

In particular, the high-Reynolds-number axial flows within fuel assemblies demand turbulence modelling strategies that optimise accuracy and computational efficiency. Large-Eddy Simulation (LES) has been widely used to resolve key turbulent structures that influence rod vibrations in axial flow [5–11]. However, the significant computational resources required by LES limit its practical application in full-scale simulations, especially when strong two-way FSI coupling is involved. In many cases, LES-derived pressure fluctuations are applied to structural solvers in a decoupled manner to predict vibration response [12–14]. While suitable for small-amplitude motion, such decoupled approaches fail to capture structural feedback on the flow, an important limitation when simulating high-Reynolds-number flows, where large vibration amplitudes can significantly alter the flow domain, especially within narrow annular gaps. One-way LES-FSI was used to predict axial-FIV responses, but the simulation became unstable for displacements corresponding to a dimensionless near-wall distance (y^+) of more than 5 [15], making such small deformation less relevant in fretting wear studies.

A more feasible alternative for simulating axial FIV involving multiple rods or entire fuel assemblies is the Unsteady Reynolds-Averaged Navier–Stokes (URANS) approach, in which turbulent Reynolds stresses are modelled rather than resolved. When coupled with a structural solver using two-way partitioned FSI coupling, this approach can capture the mutual interaction between turbulent buffeting and structural vibration, provided that the turbulence model is selected properly. In this work, we refer to this methodology as URANS-FSI.

Effective mitigation of FIV-related damage relies on accurate prediction of three key vibration parameters: natural frequency, damping ratio, and root-mean-square (RMS) amplitude, all determined from measurements of the rod's displacement. Accurate predictions of modal characteristics, including natural frequencies, mode shapes, and damping ratios, are typically obtained by applying an initial displacement or perturbation to the structure and observing the resulting free vibration decay. Frequency prediction is essential to avoid resonance, which can lead to large-amplitude instability, while identifying designs with high damping is critical for minimising fretting wear, particularly during transient events such as reactor start-up or flow interruption. The vibration frequency in axial FIV has been measured either by imposing an initial displacement [16,17] or through self-excitation by turbulent axial flow, as demonstrated at Argonne National Laboratory [18] and the University of Manchester [19–21].

URANS-FSI simulations have been shown to accurately capture both first- and second-order mode frequencies of vibration across a range of rod configurations and boundary conditions [21,22]. These include free–fixed and fixed–free configurations, validated against experimental data from the University of Manchester [21,23,24]; fixed–roller configurations, validated using experiments conducted at Vattenfall AB [25,26]; fixed–fixed configurations, validated against experimental results from Argonne National Laboratory [25,27]; and a more complex setup involving a rod positioned between four surrounding fuel assemblies based on experiments performed at Vattenfall AB [25,28].

Accurate prediction of damping ratio, particularly under high-density turbulent flow, requires strong FSI coupling to ensure numerical stability due to the large added mass effect. Damping ratios were successfully predicted using the URANS k-ω SST model [29], validated against the experiments at Argonne National Laboratory using both wall-resolved

and wall-function turbulence treatments [25,27]. However, in the case of the fixed–roller configuration from Vattenfall AB, a laminar fluid model was assumed for otherwise fully turbulent flow, yet it still achieved good agreement in the damping ratio [25]. In contrast, the application of the URANS k-ω SST model resulted in an overprediction of the damping ratio [30]. This discrepancy highlights the need for further testing and validation, particularly for this configuration, which provides a unique and realistic axial-FIV damping case while retaining geometric simplicity.

The RMS amplitude of vibration, on the other hand, can only be obtained without applying any initial displacement or perturbation, relying on self-excitation by axial turbulent flow. One of the main challenges in axial-FIV simulation using URANS is capturing flow instabilities and their effects on structural response to predict accurate rod displacements. While URANS with the eddy-viscosity-based (EVM) k-ω SST model can simulate self-sustained random vibrations, it typically underpredicts the RMS amplitude by at least two orders of magnitude compared to experiments [23,26].

To address this limitation, researchers at the Netherlands' Nuclear Research and Consultancy Group (NRG) developed the Pressure Fluctuation Model (PFM). The PFM supplements URANS by introducing additional turbulent pressure fluctuations. It generates a synthetic velocity fluctuation field using a sum of divergence-free Fourier modes, with amplitudes and spectral distributions derived from the local turbulent kinetic energy. These are used to solve the Poisson equation for pressure fluctuations, which are then superimposed onto the URANS mean pressure field to better capture unsteady structural loading [26,31]. When combined with the k-ω SST model, the PFM has shown good agreement with experimental RMS amplitudes in both cantilevered and fixed–fixed configurations under axial flow [26]. Although promising, the PFM has not yet seen widespread adoption and requires further testing and validation.

The URANS-FSI methodology presented in this paper applies the URANS approach without additional turbulence corrections such as the PFM, yet it successfully predicts all three key vibration responses: frequency, damping, and RMS amplitude. This framework, originally developed at the University of Manchester, was first validated using the Reynolds Stress Model (RSM) with the Launder–Reece–Rodi (LRR) closure. Accurate predictions were achieved for a blunt-end cantilever rod in a free–fixed configuration at an annular Reynolds number of 16.4 k [23]. The computational efficiency was improved by a factor of 40 through a geometric simplification, modelling the lead-filled rod as a hollow structure with equivalent mass concentrated in the cladding. This enabled the simulation of higher Reynolds numbers, with validation performed at 35.1 k [32].

Building on this, the framework was extended to Reynolds numbers exceeding 60k, approaching the threshold for large-amplitude flutter-like motion [21,24]. Under reversed flow (fixed–free configuration), vibration frequency was accurately predicted for both blunt- and curved-end rods. However, only the curved-end configuration correctly captured the RMS amplitude [24], while the blunt-end model significantly underpredicted it [21]. The EVM k–ω SST model was also evaluated within the same framework. For the free–fixed configuration, the model accurately reproduced RMS amplitudes consistent with the RSM LRR results. In contrast, under fixed–free conditions, it failed to sustain self-excited vibration, resulting in only small, likely non-physical deflections [21]. This behaviour resembles numerical artefacts reported by others [23,26], although in the free–fixed configuration.

This paper consolidates these findings into a comprehensive URANS-FSI simulation framework for accurately predicting modal characteristics and RMS vibration response across various rod configurations and flow conditions. The focus is on achieving robust, efficient, and validated predictions under high-Reynolds-number axial flows. Validation is performed against two key experimental benchmarks: the fixed–roller configuration from Vattenfall

AB for damping and the cantilevered rod setup from the University of Manchester for RMS amplitude. Frequency prediction is not discussed in detail, as its accuracy using URANS-FSI has already been widely demonstrated in prior studies. The following sections present the URANS-FSI methodology, describe the experimental setups, discuss key results, and conclude with best practice recommendations for future axial-FIV simulations.

2. URANS-FSI Methodology

2.1. Overview

This study employs a two-way partitioned fluid–structure interaction (FSI) approach in which the fluid and solid domains are solved separately and iteratively coupled. Both domains are discretised using the finite volume method (FVM) to maintain consistency at the interface and facilitate future integration into a monolithic solver framework. The open-source platform Foam-Extend v4.0, together with the solids4foam toolbox [33], is used for the implementation. All solvers were compiled and run in single precision to improve computational efficiency during the strongly coupled FSI procedure.

The following subsections outline the governing equations and numerical schemes applied for both fluid and solid domains.

2.2. Fluid Flow

The incompressible unsteady Reynolds-averaged Navier–Stokes (URANS) equations govern the turbulent flow field and consist of the mass and momentum conservation equations, given in Equations (1) and (2), respectively. In the Arbitrary Lagrangian–Eulerian (ALE) formulation, the mesh velocity is incorporated into the convective term, specifically the second term on the left-hand side of Equation (2), to account for the relative motion between the fluid and moving mesh boundaries, as shown below.

$$\frac{\partial U_i}{\partial x_i} = 0 \tag{1}$$

$$\frac{\partial U_i}{\partial t} + \frac{\partial}{\partial x_j}(U_i - w_i)U_j = -\frac{1}{\rho_f}\frac{\partial P}{\partial x_i} + \frac{\partial}{\partial x_j}\left(\nu\frac{\partial U_i}{\partial x_j} - \overline{u_i u_j}\right) \tag{2}$$

Here, U is the time-averaged velocity component, w is the mesh velocity, ρ_f is the fluid density, and ν is the kinematic viscosity. The Reynolds stress tensor, $-\overline{u_i u_j}$, arises from turbulence modelling in the URANS approach and contributes to the effective momentum diffusivity. The mesh velocity (w) is determined by solving a Laplacian equation, as given in Equation (3).

$$\frac{\partial}{\partial x_i}\left(\gamma\frac{\partial w_i}{\partial x_j}\right) = 0 \tag{3}$$

Here, γ is a spatially varying diffusion coefficient, set proportional to the square of the inverse distance from the interface to improve mesh quality near the solid boundary.

To improve the prediction of unsteady flow characteristics, the convective term governing the transport of momentum is discretised using the Central Difference Scheme (CDS). As an unbounded scheme, CDS minimises numerical diffusivity and is especially effective in accurately capturing large-scale flow instabilities near the rod's free end. In contrast, the convection terms in the turbulence transport equations are discretised using the first-order upwind scheme (FOUS), which is bounded and biased in the downstream direction, thereby enhancing numerical stability. Pressure–velocity coupling is handled using the Pressure-Implicit with Splitting of Operators (PISO) algorithm [34], in conjunction with Rhie–Chow interpolation adapted for dynamic meshes [35]. To ensure stability and accuracy, three PISO iterations are performed per time step.

Turbulence closure is handled within the URANS framework using two modelling approaches:

1. Eddy Viscosity Model (EVM)
2. Reynolds Stress Model (RSM)

The EVM is based on the Boussinesq approximation, which relates the Reynolds stress tensor (R_{ij}) to the mean strain rate through a turbulent viscosity (μ_t), given by

$$R_{ij} = -\rho_f \overline{u_i u_j} = \mu_t \left(\frac{\partial U_i}{\partial x_j} + \frac{\partial U_j}{\partial x_i} \right) - \frac{2}{3} \rho_f k \delta_{ij} \tag{4}$$

The eddy viscosity, μ_t, is typically derived as a function of the turbulent kinetic energy (k) and a second turbulence scale, such as the specific dissipation rate ω, where $\omega = \epsilon/k$. EVM formulations solve transport equations for k, along with either ϵ or ω, depending on the model variant. In this study, the k–ω Shear Stress Transport (SST) model [29] is employed for closure.

In contrast, the RSM provides closure by directly solving transport equations for each of the six components of the Reynolds stress tensor ($-\rho_f \overline{u_i u_j}$). The general form of these transport equations is

$$\rho_f \frac{\partial \overline{u_i u_j}}{\partial t} + \rho_f U_k \frac{\partial \overline{u_i u_j}}{\partial x_k} = \rho_f P_{ij} - \rho_f \epsilon_{ij} + \rho_f \phi_{ij} + \frac{\partial}{\partial x_k} \left[(\mu + \mu_t) \frac{\partial \overline{u_i u_j}}{\partial x_k} \right] \tag{5}$$

The production term, P_{ij}, which contributes to energy transfer among components, is defined as

$$P_{ij} = -\left(\overline{u_j u_k} \frac{\partial U_i}{x_k} + \overline{u_j u_k} \frac{\partial U_j}{x_k} \right) \tag{6}$$

The remaining terms in the Reynolds stress transport equation, namely the dissipation rate tensor (ϵ_{ij}) and pressure–strain correlation (ϕ_{ij}), are modelled following the approach by Launder, Reece, and Rodi, commonly referred to as the LRR model [36]. For practical implementation, an initial estimate of the Reynolds stress field is generated by solving the standard k–ϵ model [37] to obtain the dissipation rate ϵ and then applying the Boussinesq approximation (Equation (4)) to compute the initial stress distribution.

Near-wall turbulence is treated using standard wall functions, allowing the use of high-Reynolds-number turbulence models without resolving the viscous sublayer directly. This enables coarser mesh resolution near the wall with minimal impact on solution accuracy.

2.3. Solid Deformation

The structural domain is modelled using linear elasticity under small-strain assumptions. The governing equation is

$$\rho_s \frac{\partial^2 u_i}{\partial t^2} + [\lambda_s + \mu_s] \frac{\partial}{\partial x_i} \left(\frac{\partial u_j}{\partial x_j} \right) + \mu_s \frac{\partial^2 u_i}{\partial x_j^2} + \rho_s f_i = 0 \tag{7}$$

where u is the displacement vector; ρ_s is the solid density; λ_s and μ_s are the first and second Lam*é* constants, respectively; and f is the body force per unit mass.

To improve numerical stability, Equation (7) is rearranged as Equation (8), adopting the formulation in [38]. In this form, the second term, representing elastic and viscous deformation, is treated implicitly using linear solvers, while the third term, associated with rotational components, is handled explicitly.

$$\rho_s \frac{\partial^2 u_i}{\partial t^2} - \underbrace{[2\mu_s + \lambda_s]\frac{\partial}{\partial x_i}\left(\frac{\partial u_j}{\partial x_j}\right)}_{\text{Implicit}} - \underbrace{\frac{\partial}{\partial x_i}\left(\mu_s \frac{\partial u_i}{\partial x_j} + \lambda_s \delta_{ij}\frac{\partial u_k}{\partial x_k} + [\mu_s + \lambda_s]\frac{\partial u_j}{\partial x_j}\right)}_{\text{Explicit}} = -\rho_s f_i \quad (8)$$

Equation (8) is discretised using second-order schemes within a cell-centred finite volume method (FVM), following the approach described in [39]. The temporal term is integrated using a second-order backward Euler method, while the displacement gradient terms are discretised with a central difference scheme with non-orthogonal and skewness corrections, represented by k_{N} and k_{P} respectively. The face-normal displacement gradients are also evaluated using the central difference scheme with skewness correction, whereas the tangential components are computed using a vertex-based Gauss method, which interpolates gradients based on displacements at mesh vertices. In the cell-centred FVM approach, mesh motion is determined by calculating displacements at the cell vertices. Here, a linear least-squares method is used for cell-centre-to-vertex extrapolation, replacing the conventional inverse-distance approach to improve accuracy across varying mesh qualities [40]. The resulting discretised equation of motion forms a system of linear algebraic equations:

$$a_{\mathrm{P}} u_{i\mathrm{P}}^{[t]} + \sum_{\mathrm{N}} a_{\mathrm{N}} u_{i\mathrm{N}}^{[t]} = R_{\mathrm{P}} \quad (9)$$

a_{P} is the diagonal coefficient, a_{N} are the neighbouring coefficients presented in compact form below, and R_{P} is the source term.

$$a_{\mathrm{P}} = \frac{9\rho_f V_{\mathrm{P}}}{4\Delta t^2} + \sum_{\mathrm{f}} \left(2\mu_f + \lambda_f\right)\frac{S_{\mathrm{f}}}{\Delta x_{\mathrm{f}}} \quad (10)$$

$$a_{\mathrm{N}} = -\left(2\mu_f + \lambda_f\right)\frac{S_{\mathrm{f}}}{\Delta x_{\mathrm{f}}} \quad (11)$$

$$\begin{aligned} R_{\mathrm{P}} = \rho_{\mathrm{f}} V_{\mathrm{P}} &\left[\frac{3u_{i,\mathrm{P}}^{[t-1]}}{\Delta t^2} - \frac{3u_{i,\mathrm{P}}^{[t-2]}}{4\Delta t^2} + \frac{2}{\Delta t}\left(\frac{\partial u_i}{\partial t}\right)_{\mathrm{P}}^{[t-1]} - \frac{1}{2\Delta t}\left(\frac{\partial u_i}{\partial t}\right)_{\mathrm{P}}^{[t-2]}\right] \\ &- \sum_{\mathrm{f}} (2\mu_{\mathrm{f}} + \lambda_{\mathrm{f}})\left[k_{\mathrm{N},j}\left(\frac{\partial u_i}{\partial x_j}\right)_{\mathrm{N}}^{[t]} - k_{\mathrm{P},j}\left(\frac{\partial u_i}{\partial x_j}\right)_{\mathrm{P}}^{[t]}\right]\Delta x_{\mathrm{f}} S_{\mathrm{f}} \\ &+ \sum_{\mathrm{f}} n_{\mathrm{f},j} q_{\mathrm{f},j}^{[t]} S_{\mathrm{f}} + \rho_{\mathrm{f}} b_{\mathrm{P},i}^{[t]} V_{\mathrm{P}} \end{aligned} \quad (12)$$

S_{f} represents the surface area at the cell face (f), V_{P} is the volume of the control volume (P), q is the explicitly treated term in the solid governing equation of motion (Equation (8)), and b is the source term such as gravity. A segregated algorithm is employed, where the displacement components in the x-, y-, and z-directions are solved separately and then recoupled through fixed-point iterations. Fine-tuning this inter-component coupling in a solid-only free vibration simulation has been shown to enhance the computational efficiency of the solver while maintaining stability and accurately predicting the vibration response, particularly the frequency [32].

2.4. Fluid–Structure Interaction Coupling

At the FSI interface, strong coupling between the turbulent flow and structural vibration is achieved using the DN–decomposition approach, a method commonly employed in strongly coupled FSI simulations. The coupling procedure begins by enforcing continuity

of displacement or velocity (Equations (13) and (14)), also known as the Dirichlet boundary condition, followed by continuity of traction forces (Equation (15)), corresponding to the Neumann boundary condition.

$$U_{f,i} = U_{s,i} = \frac{du_{s,i}}{dt} \tag{13}$$

$$u_{f,i} = u_{s,i} \tag{14}$$

$$n_i \sigma_{f,i} = n_i \sigma_{s,i} \tag{15}$$

In the segregated FSI algorithm, where the fluid and solid domains are solved using separate solvers, a residual arises between the predicted solid displacement, based on fluid traction from the previous time step, and the current fluid mesh displacement at the FSI interface. This difference defines the FSI residual, **r**, as expressed in Equation (16).

$$\mathbf{r}_i^k = \mathbf{u}_{s,i}^k - \mathbf{u}_{f,i}^k \tag{16}$$

where the subscript i denotes vertices at the FSI interface.

As illustrated in Figure 1, within each FSI coupling loop, the fluid mesh displacement at the interface is estimated. The fluid solver is then executed, and the resulting traction forces at the FSI interface are interpolated onto the solid surface. The FSI residual (defined in Equation (16)) is calculated and checked against convergence criteria, which include both tolerance (Tol-FSI) and a limit on the number of FSI iterations (nOuterCorr). Once these criteria are satisfied, the simulation advances to the next time step. Non-conformal mesh interfaces between the fluid and solid domains are managed using the Generalised Grid Interface (GGI) interpolation method [39].

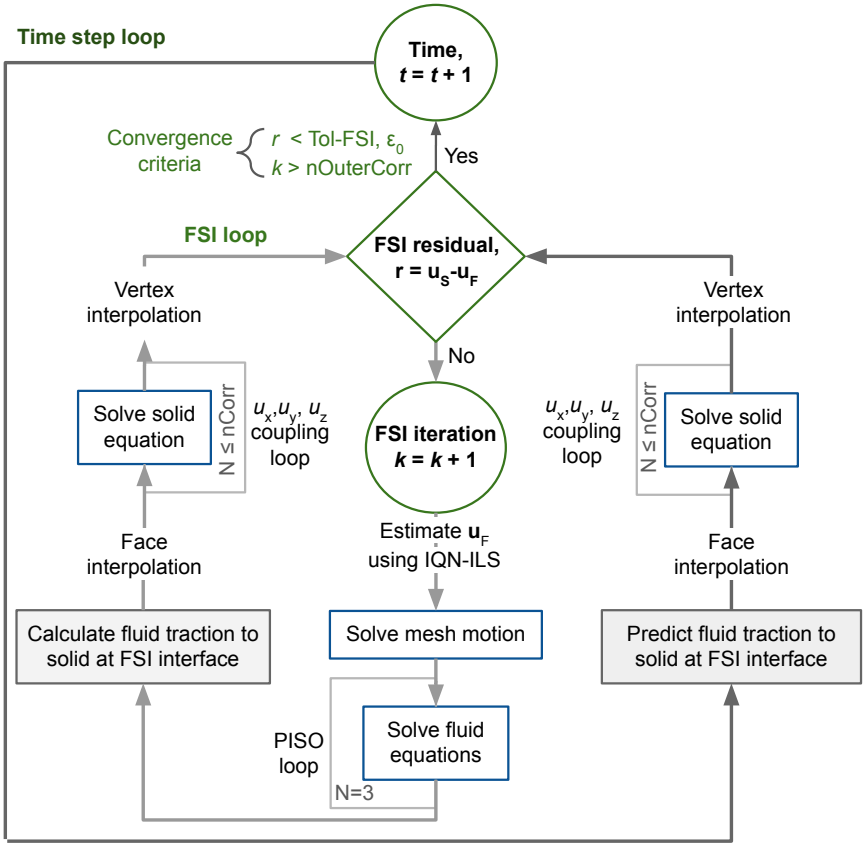

Figure 1. Overview of FSI coupling algorithm.

To prevent numerical instabilities associated with numerical added mass effect and to maintain simulation continuity without divergence, particularly when resuming the simulation during interruption, as reported in other partitioned FSI studies [23,41], a very low relaxation factor of 0.05 is applied to the displacement of fluid mesh vertices during initial FSI iterations. This is followed by the application of an FSI coupling acceleration method, such as the interface quasi-Newton method with inverse least-squares approximation (IQN-ILS) to accelerate the convergence of the FSI residual [42]. The IQN-ILS method constructs update matrices using the solid displacement and interface residuals from previous FSI iterations and time steps. However, due to the high-frequency structural response driven by turbulent buffeting, only data from the most recent time step is retained to ensure numerical stability. Using data from multiple prior time steps was found to reduce overall simulation robustness.

3. Empirical Model by Païdoussis (1966)

An empirical model to predict the vibration amplitude in axial FIV was presented by Païdoussis through systematic trial and error, incorporating physical insights from experimental data provided by Burgreen et al. [43], Quinn [44], Société Grenobloise d'Applications Hydrauliques (SOGREAH) [45], and Roström and Andersson [46]. He proposed an empirical expression to predict the amplitude of small-amplitude random vibrations of a single rod or rod bundle in axial flow, supported at both ends, as expressed in Equation (17).

$$\frac{y_{\max}}{d_{\mathrm{ro}}} = \alpha_1^{-4}\left[\frac{\widetilde{U}^{1.6}\epsilon^{1.8}Re_{\mathrm{ann}}^{0.25}}{1+\widetilde{U}^2}\right]\left[\left(\frac{d_{\mathrm{h}}}{d_{\mathrm{ro}}}\right)^{0.4}\right]\left[\frac{\beta_{\mathrm{mass}}{}^{2/3}}{1+4\beta_{\mathrm{mass}}}\right]\left[5\times10^{-4}K\right] \tag{17}$$

$y_{\max}$, d_{ro}, d_{h} and Re_{ann} represent, respectively, the maximum amplitude of vibrations, the rod's diameter, the hydraulic diameter of the annulus, and the annulus Reynolds number. The dimensionless variables $\widetilde{U}$, α_1, ϵ_L, β_{mass}, and K are defined as follows:

1. Dimensionless flow velocity, $\widetilde{U}$, is defined based on the geometrical (cross-sectional area, A_{rod}, length, L_{rod}, and second moment of area, I_{rod}) and material (Young's modulus, E) properties of the vibrating rod, as given in Equation (18). The bracketed term in Equation (18) corresponds to the FSI-modified Cauchy number.

$$\widetilde{U} = \frac{A_{\mathrm{rod}}L_{\mathrm{rod}}^2}{I_{\mathrm{rod}}}\left(\frac{\rho_f U_{\mathrm{ann}}^2}{E}\right)^2 \tag{18}$$

2. Departure from ideal fixture, α_1 or also known as the first mode of eigenvalue of the system [47], in which, for rods with simply hinged on both ends, $\alpha_1 = \pi$, and for rods fixed at both ends, $\alpha_1 = 4.71$. For other boundary conditions, α_1 is defined based on the rod's material and geometric properties, as well as the angular frequency of oscillation, ω, and is given by the following expression (Equation (19)):

$$\alpha_1^2 = \left[\frac{(\rho_f A_{\mathrm{rod}} + \dot{m}_{\mathrm{rod}})L_{\mathrm{rod}}^4}{EI}\right]^{1/2}\omega \tag{19}$$

3. Length-to-diameter ratio, ϵ_L, is given as ratio of rod's length over its diameter, $L_{\mathrm{rod}}/d_{\mathrm{ro}}$.
4. Added mass ratio, β_{mass}, is defined as the ratio of the mass of fluid displaced by the immersed rod ($\dot{m}_{\mathrm{add}}$) to the combined mass of the rod and the displaced fluid, $\dot{m}_{\mathrm{add}}/(\dot{m}_{\mathrm{add}} + \dot{m}_{\mathrm{rod}})$.
5. Noise factor, K, where $K = 1$ represents quiet laboratory conditions and $K = 5$ represents typical industrial conditions.

Although originally developed for rods supported at both ends, the empirical model was fitted to a blunt-end cantilever and showed good agreement with both experimental measurements and URANS-FSI simulations [21], particularly within the small-amplitude random vibration regime (see Figure 2). Two assumptions were made in applying Equation (17): firstly, the maximum displacement was taken to be equal to the RMS amplitude ($y_{max} = A_{rms}$) and secondly, the noise factor was assumed to correspond to a quiet laboratory environment ($K = 1$).

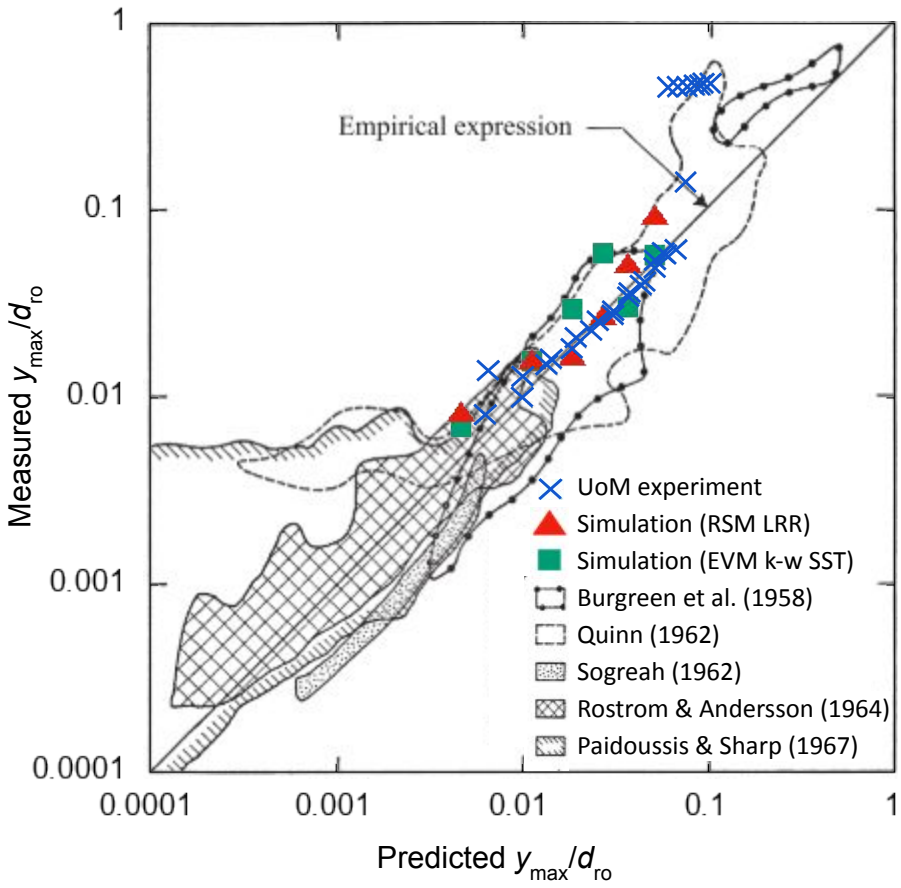

Figure 2. Comparison between experimental data and URANS simulation results for the blunt-end free–fixed configuration [21] and predictions from the empirical model by Païdoussis [47]. The figure also includes data from other relevant experiments on small-amplitude vibrations in axial FIV, as compiled by Païdoussis [48]; Burgreen et al. [43], Quinn [44], SOGREAH [45], Rostrom and Andersson [46], and Païdoussis and Sharp [49].

4. Damping in Axial FIV

4.1. Fixed–Roller Case at Vattenfall

This case uses a simplified geometry, a square beam within a square duct to validate damping ratio for simulating vibrations in a high-stiffness solid domain under axial water flow. The simulation results are compared against experimental data from Vattenfall AB, as reported in [16].

The experimental setup and schematic are shown in Figure 3. It consists of a long rectangular steel beam submerged in a square flow duct, with water entering from the bottom and exiting at the top. The beam is clamped at the upstream end, while its motion in the xy-plane is constrained by a downstream roller. At the midpoint (point B), a string is attached to apply an initial transverse displacement of 0.01 m in the y-direction. The string is then released, and the resulting displacement response is measured to assess the vibration. The material and geometrical properties of the solid and fluid domains are

listed in Tables 1 and 2, respectively. The bulk Reynolds number is computed based on the hydraulic diameter d_h, defined along the axis of the initial displacement.

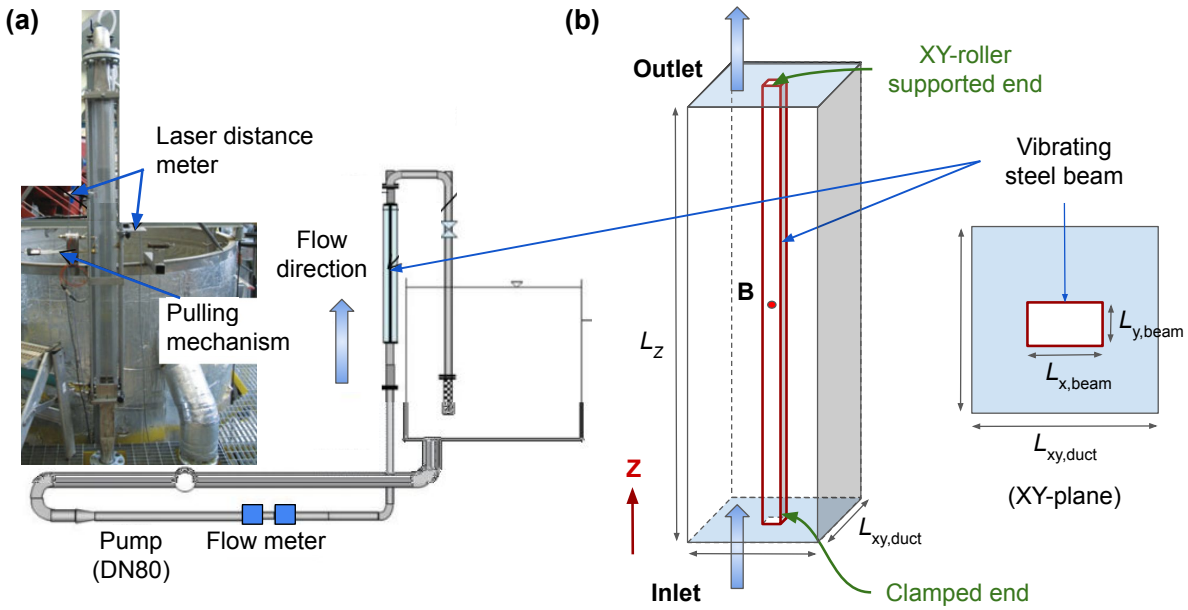

Figure 3. (**a**) Experimental setup [16] and (**b**) simulation domain for the Vattenfall vibration in the axial flow case.

Table 1. Material and geometrical properties for the Vattenfall fixed–roller supported rod, based on the experimental setup reported in [16].

Properties		Values
Materials	Density, ρ_s [kg/m^3]	8000
	Young's Modulus, E [N/m^2]	193×10^9
	Poisson's ratio, ν_s	0.3
Geometrical	Width, L_x (beam) [m]	0.02
	Height, L_y (beam) [m]	0.008
	Length, L_z [m]	1.5

Table 2. Fluid and geometrical properties of the Vattenfall flow channel.

Properties		Values
Fluid	Density, ρ_f [kg/m^3]	1000
	Kinematic viscosity, ν [m^2/s]	1.0
	Dynamic viscosity, μ [kg/(m·s)]	0.001
	Bulk flow velocities, U_z [m/s]	1.0, 3.0
	Bulk Reynolds number, Re_b	36 k, 108 k
Geometrical	Width, $L_{x,\text{duct}}$ [mm]	0.08
	Height, $L_{y,\text{duct}}$ [mm]	0.08
	Length, L_z [m]	1.5
Frequency	In vacuum [Hz]	12.4
	In quiescent water [Hz]	11.7

4.2. Mesh and FSI Coupling Sensitivity

To establish a reliable numerical setup, a preliminary mesh and time-step independence study was performed on the solid domain in isolation. A free vibration test was conducted to validate the natural frequency and to verify that no damping occurred,

as expected in a vacuum environment, where any observed damping would result from numerical artefacts rather than physical effects. In parallel, the convergence criteria for the solid solver were carefully tuned to ensure both accuracy and computational efficiency. Description of the solid domain is given in Table 3.

Table 3. Description of time-step size, solid mesh, solid solvers, and FSI coupling for the Vattenfall case.

Properties	Values
Time-step size, Δt [s]	10^{-4}
Solid mesh	
Width intervals, Nx [Intervals]	3
Height intervals, Ny [Intervals]	6
Longitudinal intervals, Nz [Intervals]	640
Solid solver	
Linear solver tolerance	10^{-9}
Inter-component coupling tolerance, Tol-s	10^{-7}
Inter-component coupling limit number of iterations, nCorr [Iterations]	1000
FSI coupling	
FSI coupling algorithm	Gauss Seidel/ IQN-ILS
FSI relaxation	0.05
FSI convergence tolerance, Tol-FSI	10^{-6}
Limit number of FSI iterations, nOuterCorr [Iterations]	30
Number of time steps reusing coupling information	0

To ensure mesh independence, a sensitivity study was conducted for axial flow at a bulk Reynolds number of 36 k using the EVM k-ω SST model [29]. The mesh was first refined in the longitudinal direction, followed by additional refinement in the xy-plane for both Reynolds numbers of 36 k and 108 k.

As shown in Figure 4a, the coarse longitudinal mesh predicts a slightly higher vibration frequency and greater damping than the experiment. Increasing the number of longitudinal intervals reduces these differences and brings the solution closer to the experimental measurement. The first displacement peak occurs at $t \approx 0.095$ s, with time difference remaining below 3% for all refined meshes. The peak-amplitude error also decreases steadily with refinement, and by 1280 intervals, the error fall within 10% of the experimental value. This mesh was therefore chosen for the remaining simulations, offering a 62.4% reduction in computational time compared with the 2560 intervals. Following the ASME V&V 20-2009 standard [50], a three-mesh grid convergence index (GCI) analysis of the axial refinement gives numerical uncertainties of 0.13% for the peak-time and 2.22% for the peak-amplitude response, confirming that discretisation effects in the longitudinal direction have only a limited influence on the predicted response.

Figure 4b,c shows that mesh refinement in the xy-plane produces only minor changes in the displacement response for both flow speeds. The time difference of the first peak remains below 3% to the experimental value, and the peak-amplitude differences across all transverse meshes remained within 10%. A corresponding GCI estimate for the transverse refinement gives uncertainties below 0.2% for both timing and amplitude, indicating that numerical uncertainty in the xy-plane. Overall, these results indicate that the vibration response is only weakly affected by the transverse resolution, and that the coarse xy-plane mesh is sufficient to achieve mesh independence.

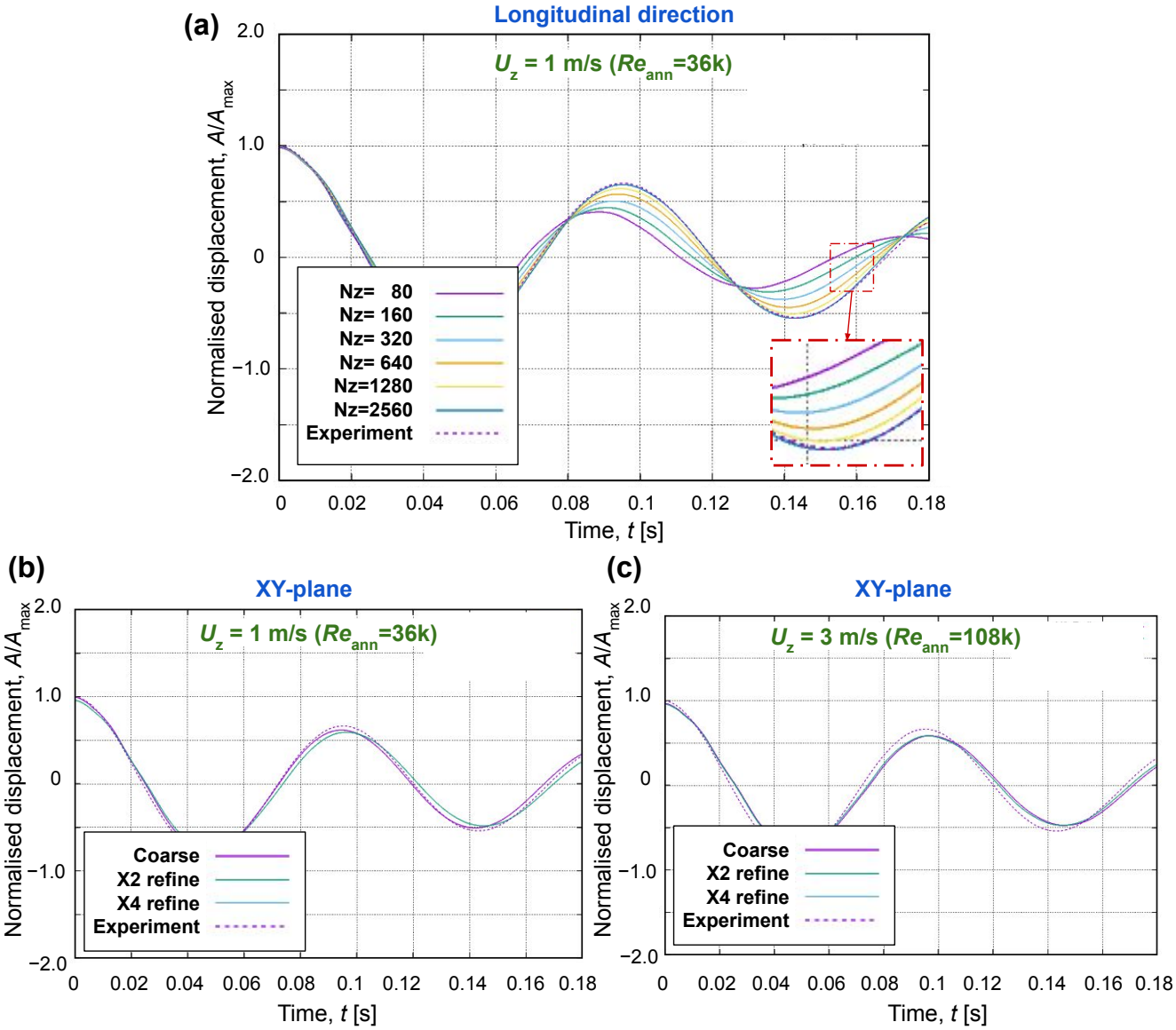

Figure 4. Displacement time series of vibration in axial flow at a bulk Reynolds number of 36 k. Panel (**a**) shows the sensitivity to longitudinal mesh resolution (Nz) ranging from 80 to 2560. Panels (**b**,**c**) show the effect of mesh refinement in the XY-plane—coarse (15 × 15), ×2 refinement (30 × 30), and ×4 refinement (60 × 60)—at bulk Reynolds numbers of 36k and 108k, respectively, for the Vattenfall case.

A comparison was conducted between the current IQN-ILS coupling algorithm and the Gauss-Seidel algorithm with Aitken relaxation. Both FSI coupling strategies yielded nearly identical predictions of vibration frequency and amplitude when compared with the experimental data. However, the IQN-ILS algorithm reduced the number of iterations to reach convergence as shown in Figure 5 and achieved faster computation time than the Gauss–Seidel with Aitken approach. This finding is consistent with previous studies [42,51], which demonstrated the superior efficiency of IQN-ILS in simulating axial FIV of flexible rods across a range of solid-to-fluid density ratios.

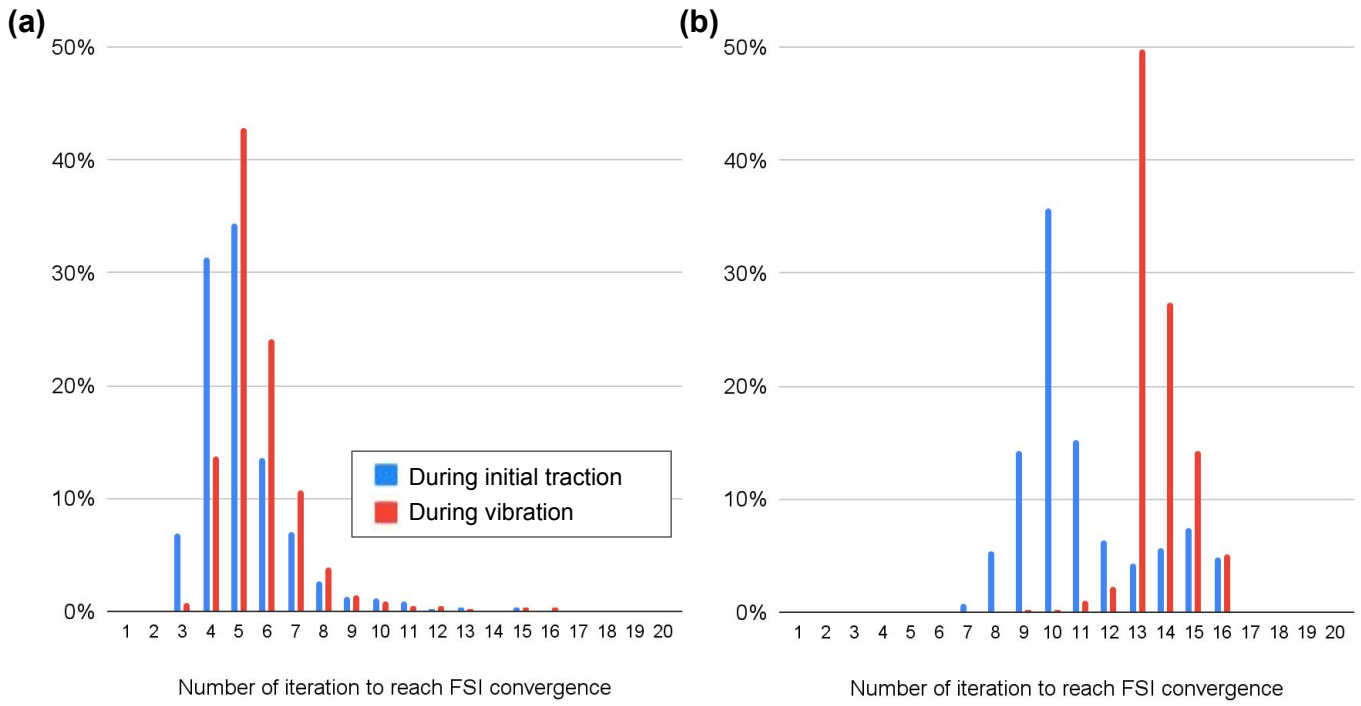

Figure 5. Comparison of the number of FSI coupling iterations required to reach convergence (nOuterCorr) for the Vattenfall case at a bulk Reynolds number of 36k in axial flow. Panel (**a**) shows results using the IQN-ILS algorithm, while panel (**b**) presents results using the Gauss–Seidel method with Aitken relaxation. Each bar shows the percentage of time steps requiring a given number of iterations to reach convergence during the initial traction phase (blue) and during vibration (red).

4.3. Comparing URANS Models

Simulations were repeated for axial flows at bulk Reynolds numbers of 36 k and 108 k using three fluid models: the commonly used EVM k-ϵ model [37], the baseline EVM k-ω SST model [29], and a laminar flow model previously employed [25,26]. Although the laminar model is not physically representative at these Reynolds numbers, earlier studies showed that it can still predict vibration damping with reasonable accuracy. Including it here therefore allows direct comparison with previous validation work and highlights the improvement gained by applying URANS models to this case for the first time.

A similar study on vibration damping in axial flow was performed at a similar flow velocity, with the fluid viscosity varied to set the annulus Reynolds number to 1000 for the laminar case and 80,000 for the turbulent case. They observed weaker damping in turbulent case compared with the laminar case, attributing this to enhanced surface pressure fluctuations driven by vorticity [7]. In the present study, larger cell sizes failed to resolve near-wall vorticity accurately, resulting in overestimated damping due to dominant laminar flow components, not accounted for by the turbulent eddies. Finer meshes, however, captured pressure fluctuations more accurately and produced damping values consistent with experimental results.

Figure 6 compares the displacement time series for the damping of vibration in axial flow at a bulk Reynolds number of 36 k. All three models show good agreement with the experimental results, with the laminar model standing out for its computational efficiency, running approximately three times faster than the URANS models. The first displacement peak occurs at $t \approx 0.095$ s for all models, with timing differences below 2%. The normalised peak amplitudes differ by less than 8% between the models and the experiment, indicating only minor sensitivity of the predicted response to the choice of flow model.

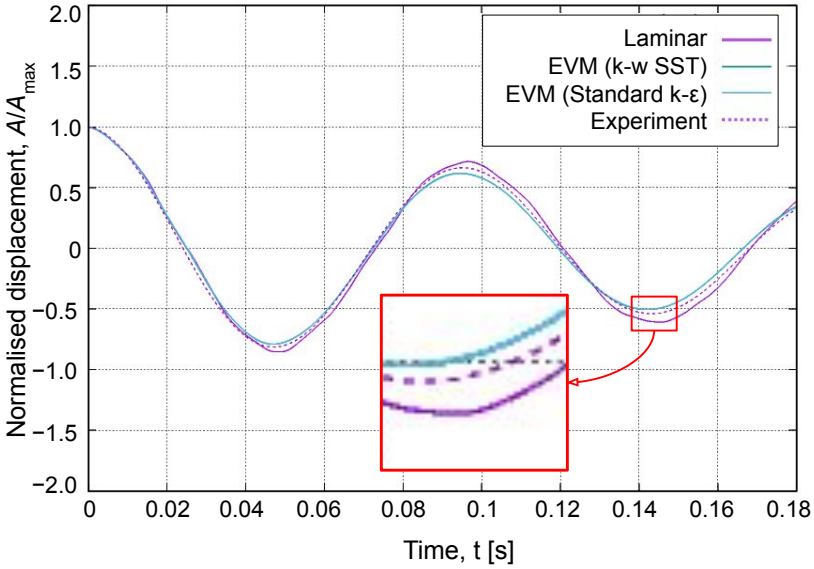

Figure 6. Displacement time series of vibration for different flow models for Vattenfall vibration in bulk Reynolds number of 36k axial flow.

To investigate the mechanisms behind vibration damping, contour plots of dimensionless velocity (U/U_{in}) and pressure coefficient (C_p) were analysed for both laminar and URANS k-ω SST models in the xy- and yz-planes.

Figure 7a shows the velocity contours in the xy-plane. Both models exhibit similar internal flow structures, with high velocity gradients near the walls. However, the laminar model shows slightly higher velocity along the vibration axis (y-axis), while the URANS model produces a more uniform distribution due to turbulence mixing.

In Figure 7b, pressure contours reveal that the laminar model exhibits high pressure on one side of the beam, with a sharp transition as the beam reverses direction between 0.06 s and 0.07 s. In contrast, the URANS model shows a more gradual pressure redistribution, consistent with more realistic flow physics near oscillating surfaces.

Figure 8 presents flow contours in the yz-plane at various axial positions. Velocity distributions are broadly similar near the fixed and roller-supported ends. At the beam's mid-span, however, the URANS model shows peak velocities near the beam's wider clearance, while the laminar model's peak appears mid-gap. Pressure profiles are generally consistent between the two models, but the laminar model displays unrealistic pressure variation along the beam, suggesting numerical artefacts in the absence of turbulence modelling. The URANS model, by contrast, captures a peak pressure near the mid-span where flow constriction occurs, consistent with expected physical behaviour.

Despite the laminar model's neglect of turbulence, it still captures vibration damping reasonably well, primarily due to its heightened sensitivity to flow disturbances and pressure asymmetries. In contrast, the URANS model dampens vibration through turbulent mixing, vortex shedding, and enhanced kinetic energy near the beam surface, resulting in damping behaviour that aligns more closely with experimental observations.

In summary, while the laminar model underpredicts flow detail and generates some unrealistic pressure behaviour, it provides a fast and reasonably accurate prediction of vibration damping. The URANS model offers improved physical realism at higher computational cost, making it preferable for capturing detailed flow–structure interactions in axial FIV.

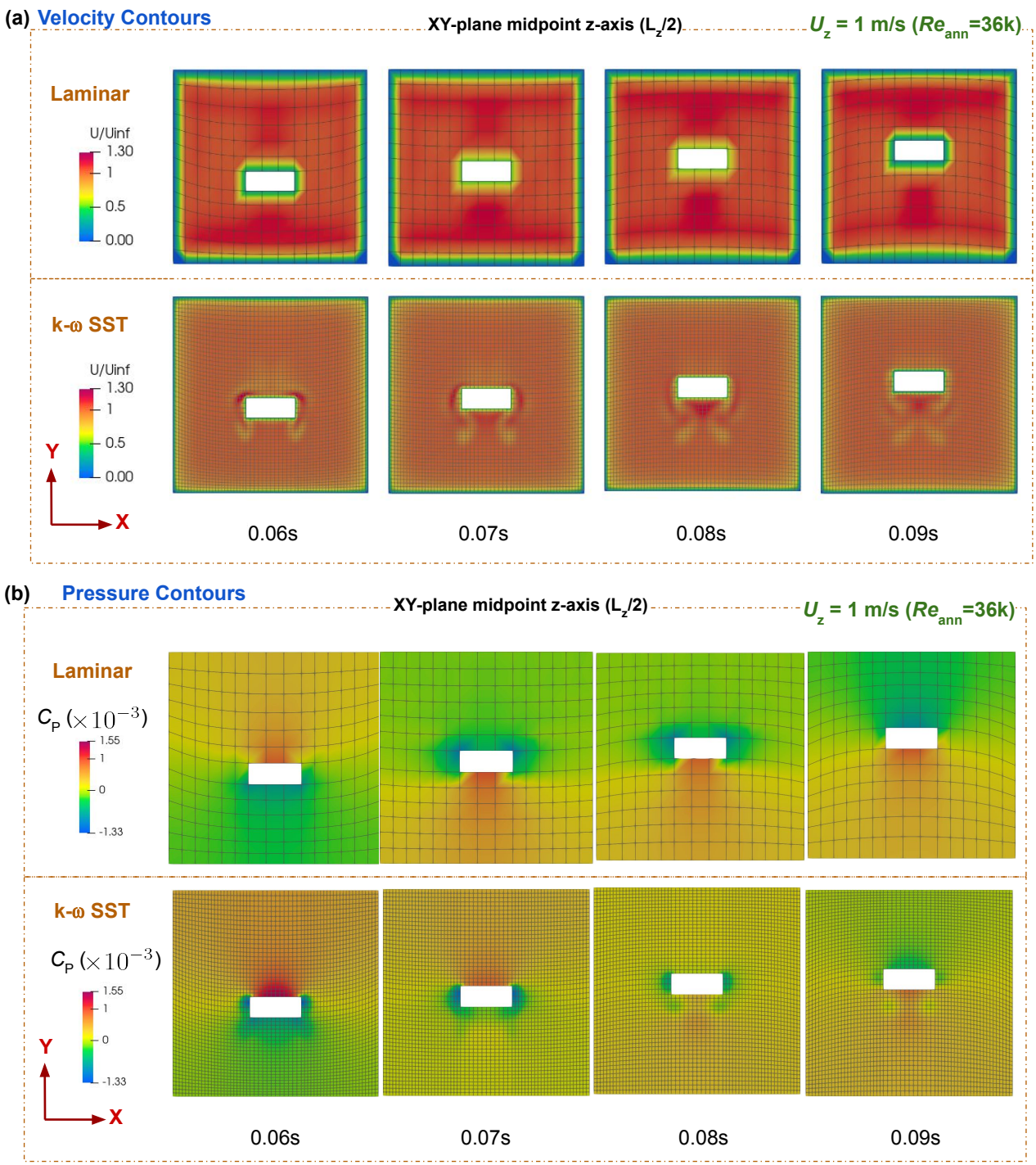

Figure 7. Comparison of the (**a**) velocity and (**b**) pressure contour plots at the axial midpoint in the xy-plane for different fluid models: laminar (top) and URANS k-ω SST (bottom), at various times (referred to Figure 6), for the Vattenfall vibration in bulk Reynolds number of 36 k axial flow case.

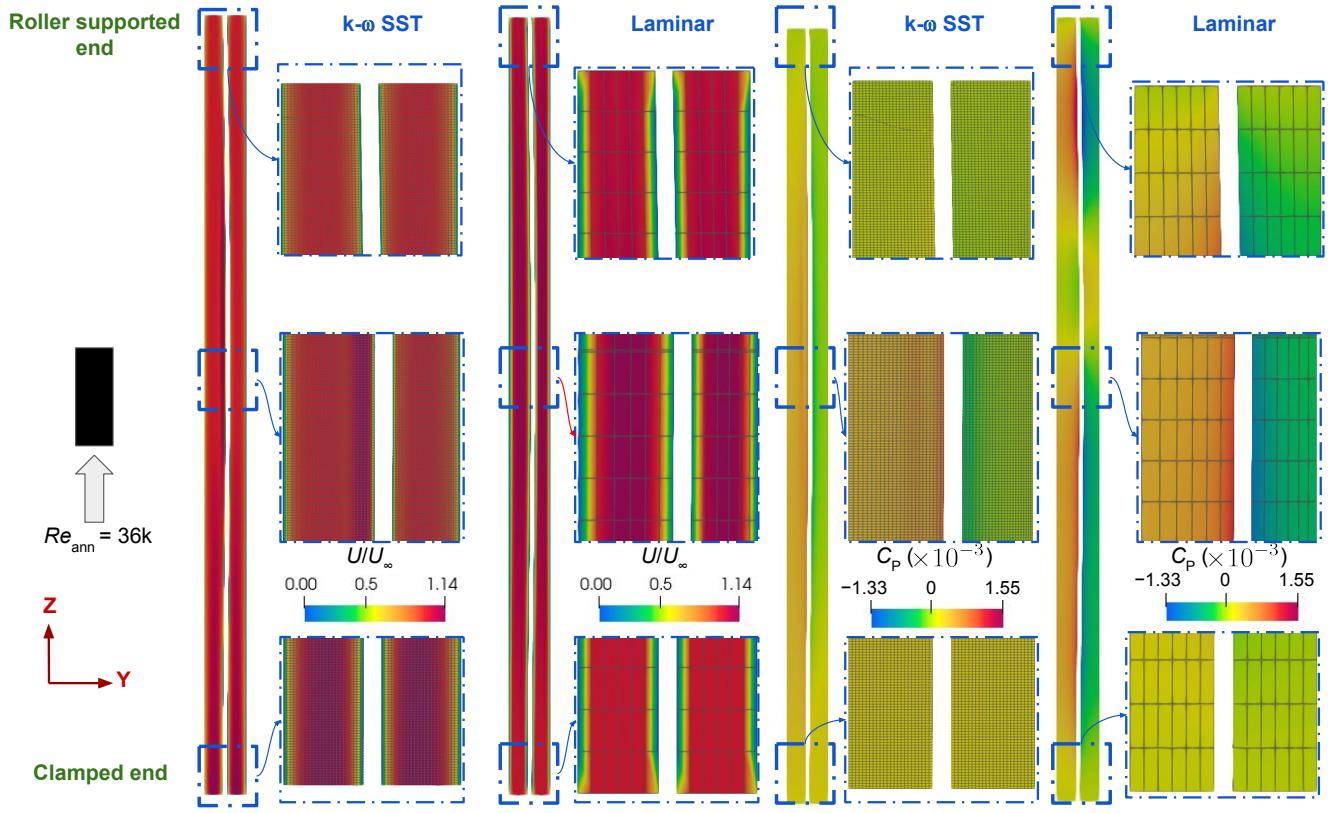

Figure 8. Comparison of the contour plots at midpoint axially in the yz-plane with different fluid models; URANS k-ω SST and laminar, during a vibration peak (referred to 0.09 s in Figure 6) for the Vattenfall vibration in bulk Reynolds number of 36 k axial flow case.

5. Root-Mean-Square Amplitude in Axial FIV

5.1. Cantilever Rod Case at University of Manchester (UoM)

The RMS vibration amplitude is validated against experimental data from an axial-FIV setup involving a cantilevered rod in an annular flow channel. Figure 9a presents the schematic of the test section, while the flow domain parameters are provided in Table 4. Figure 9b shows the cantilever rod, with its dimensions detailed in Table 5.

Table 4. Fluid and geometrical properties of the UoM case.

Properties	Values					
Fluid						
Density, ρ_f [kg/m^3]	997.84					
Kinematic viscosity, ν [m^2/s]	9.659×10^{-4}					
Dynamic viscosity, μ [kg/(m·s)]	9.68×10^{-7}					
Inlet conditions						
Annulus Reynolds number, Re_{ann}	16.4 k	26.5 k	35.1 k	43.1 k	51.3 k	61.7 k
Average annular velocity, U_{ann} [m/s]	1.32	2.27	3.09	3.46	4.11	4.94
Average inlet velocity, U_{in} [m/s]	1.02	1.71	2.39	2.67	3.17	3.82
Geometrical						
Tube diameter, d_{ti} [mm]	21.0					
Hydraulic diameter, d_h [mm]	11.0					

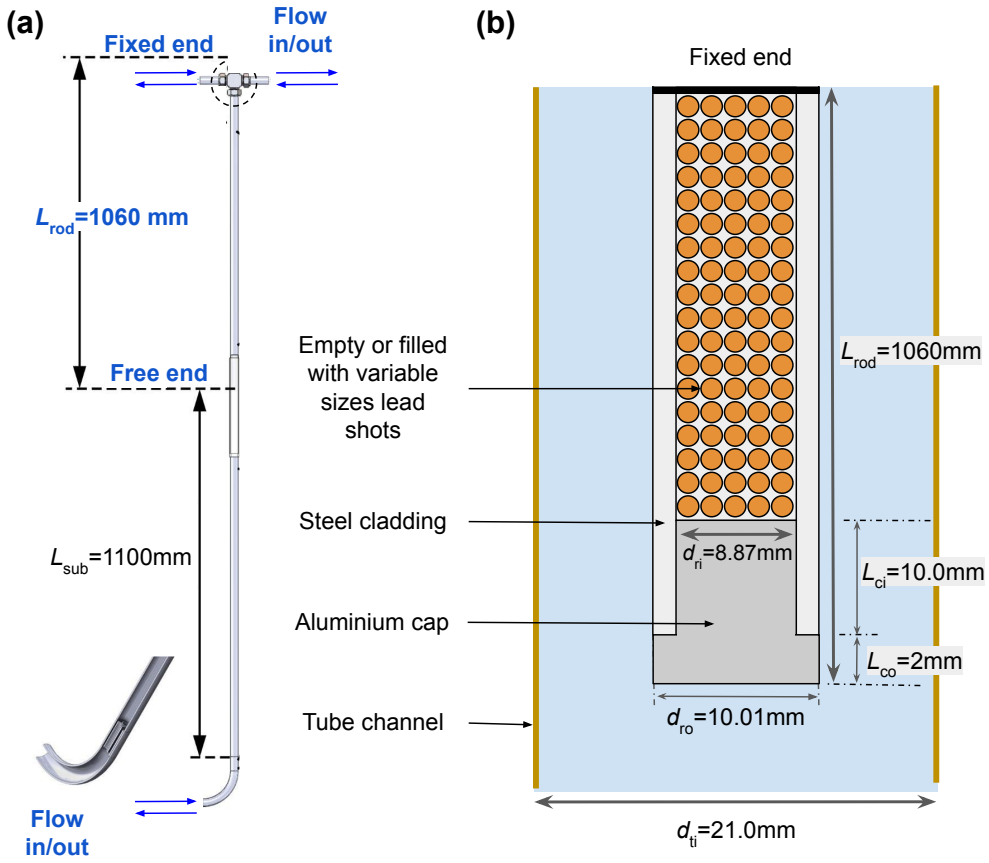

Figure 9. Schematic of (**a**) the test piece section and (**b**) details of cantilevered rod for the UoM experiment.

Table 5. Material and geometrical properties for the UoM cantilever rod, based on the experimental specifications reported in [19,21].

Properties	Values
Materials	
Young's modulus, E_{steel} [GPa]	193
Rod density, ρ_{steel} [kg/m^3]	7990
Rod (lead-filled) linear mass density, $\dot{m}_{rod}$ [kg/m]	0.588
Lead density, ρ_{lead} [kg/m^3]	11,340
Lead filling density, ρ_{fill} [kg/m^3]	9.6
Cap density, ρ_{alu} [kg/m^3]	2740
Cap mass, m_{alu} [g]	2.1
Geometrical	
Rod outer diameter, d_{ro} [mm]	10.01
Rod inner diameter, d_i [mm]	8.83
Rod length, L_{rod} [mm]	1060
Lead shot diameter, d_{shot} [mm]	0.3–1.6
Cap inner length, L_{ci} [mm]	10.0
Cap outer length, L_{co} [mm]	2.0

The fluid domain in Figure 10 is first validated by comparing velocity profiles at the inlet and near the free end with PIV measurements [21]. A mesh independence study was conducted for both the fluid and solid domains. In the fluid domain, radial refinement at the annulus wall (Nr-ann) was applied to better resolve curvature, while increasing circumferential intervals (Nc) helped reduce aspect ratios and enhance numerical stability. Additionally, the axial mesh near the free end (dz-free) was refined over a length of one

tube diameter (d_{ti}) from the tip, as this region is critical for capturing flow-induced forces and vibration response [11].

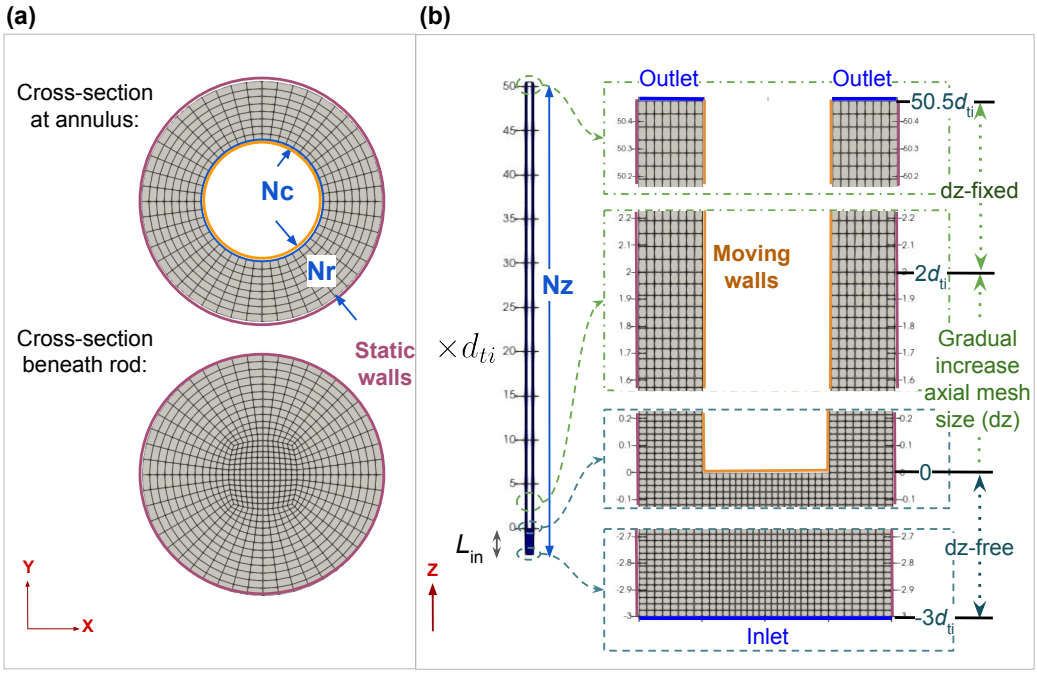

Figure 10. Fluid mesh view of the flow channel definition in (**a**) xy-plane and (**b**) yz-plane for the UoM case.

For the solid domain in Figure 11, mesh independence was assessed through a free vibration test using an empty tube rod. Circumferential (Nc), radial (Nr), and axial (Nz) mesh intervals were fine-tuned by comparing the undamped vibration response against analytical results from Euler–Bernoulli beam theory. The lead-filled rod was modelled as a hollow structure with equivalent linear mass density by concentrating mass in the cladding, significantly improving computational efficiency over the solid model [32].

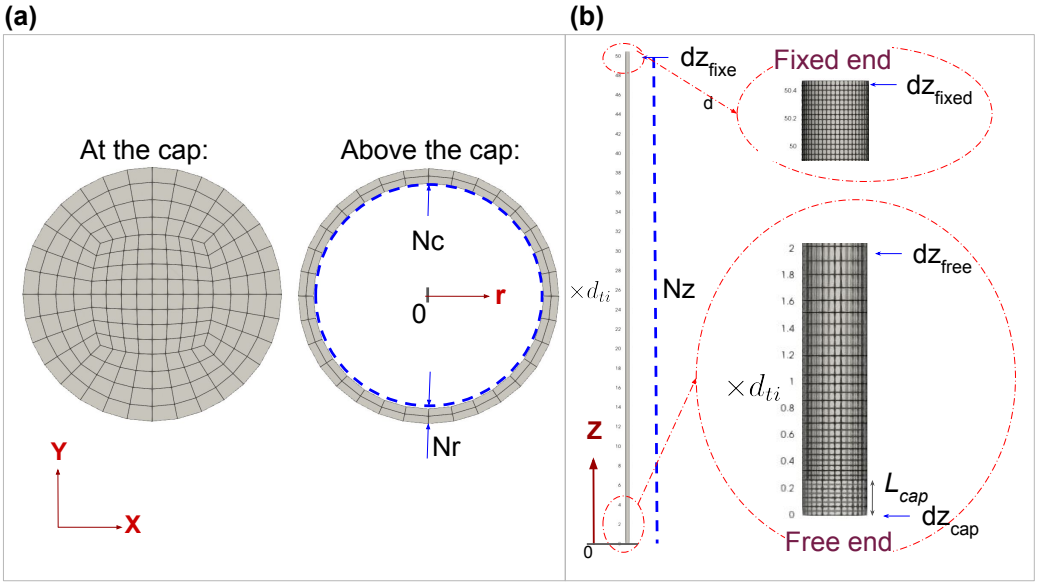

Figure 11. Solid mesh view in (**a**) xy-plane and (**b**) yz-plane for the UoM case.

As summarised in Figure 12, the validation process for the self-excited axial-FIV simulations began with simplified geometry cases, including the Vattenfall vibration in the axial flow case, to assess and refine solver settings prior to full two-way FSI coupling.

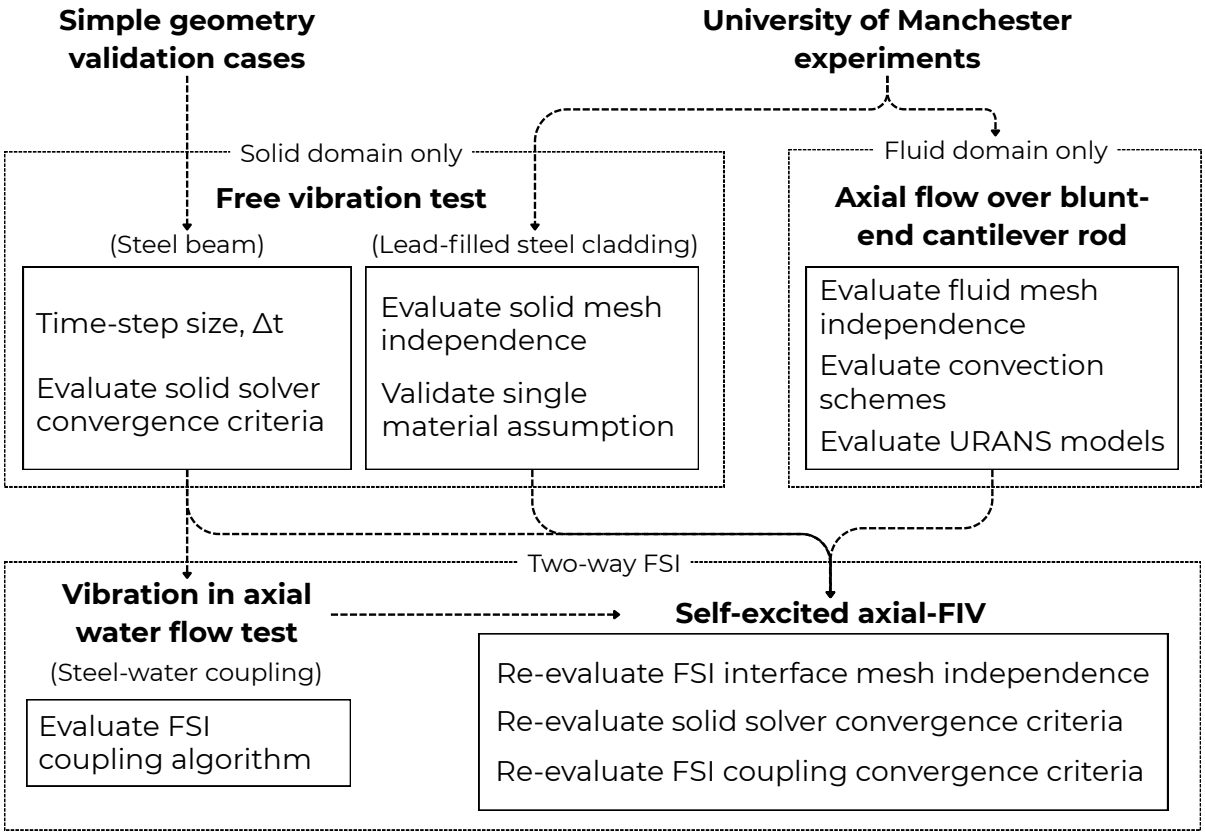

Figure 12. Summary of the URANS-FSI validation and fine-tuning strategy for axial-FIV simulation.

To enhance efficiency without compromising accuracy, the solid solver tolerance was set to 10^{-7}, and the iteration limit (nCorr) was reduced from 1000 (used in the free vibration case) to 125 for the self-excited axial-FIV simulation, resulting in significant speed-up with minimal impact on RMS amplitude and vibration frequency. For FSI coupling, initial validation from the Vattenfall vibration in axial flow case employed a relaxation factor of 0.05 and a tolerance of 10^{-6}, which was later fine-tuned to 10^{-4} for the self-excited axial-FIV case. The maximum number of FSI iteration (nOuterCorr) was reduced from 30 to 20, which was sufficient, as higher values provided no accuracy gains. Mesh sensitivity tests showed that finer circumferential grading (such as Nc = 48) improved FSI convergence and computational stability, though at the cost of increased computational time due to mesh size. To avoid instability, the IQN-ILS algorithm's reuse of interface data was restricted to a single previous time step.

Table 6 tabulates the meshes and the fine-tuned convergence criteria for the fluid, solid, and FSI solvers.

Simulations began with validation against tip displacement under axial water flow at the mid-range annular Reynolds number of 35.1 k.

Figure 13 compares the displacement time series from the 60 s experiment with the 5 s simulation. Both URANS models, EVM k-ω SST and RSM LRR, predict small-amplitude random vibrations about the centreline, consistent with experimental observations. The RSM LRR model produces a higher RMS amplitude than the EVM k-ω SST model, attributed to the latter's stronger turbulence damping, which suppresses flow instabilities and thus underpredicts vibration amplitude. Occasional transient deflections are

observed in both simulation and experiment, though vibrations generally remain centred. Given the randomness of the vibration, comparing the resultant RMS displacement offers a clearer assessment, with both models showing acceptable agreement. The RSM LRR model gives about 25% higher than the experiment, while the EVM k-ω SST model underpredicts it by roughly 35%. These differences are typical for self-excited, turbulence-driven vibration and remain within the expected variability reported in axial-FIV studies [23,26]. To support transparency and reproducibility, the OpenFOAM case files for both models are available in an online repository [52].

Table 6. Description of time-step size, fluid mesh, solid mesh, solid solver and FSI solver for UoM case.

Properties	Values
Time-step size, Δt [s]	10^{-4}
Fluid mesh	
Radial intervals, Nr-ann [Intervals]	8–10
Circumferential intervals, Nc [Intervals]	32–48
Axial intervals, Nz [Intervals]	1218–1470
Axial mesh ratio, dz-ratio	2 or 4
Solid mesh	
Radial intervals in cladding, Nr [Intervals]	2
Circumferential intervals, Nc [Intervals]	32–48
Axial mesh ratio, dz-ratio	0.25
Solid solver	
Linear solver tolerance	10^{-9}
Inter-component coupling tolerance, Tol-s	10^{-7}
Inter-component coupling iteration limit, nCorr [Iterations]	125
FSI coupling	
FSI coupling algorithm	IQN-ILS
FSI relaxation	0.05
FSI convergence tolerance, Tol-FSI	10^{-4}
Limit number of FSI iterations, nOuterCorr [Iterations]	20
Number of time steps reusing coupling information	0 or 1

Additionally, for a similar setup with a curved-end geometry, it was reported that only the RSM LRR model accurately captured the RMS amplitude. In contrast, the EVM k-ω SST model exhibited sustained small-amplitude vibrations but with RMS values several orders of magnitude lower than those measured experimentally [24].

Figure 14 presents the cumulative moving average (CMA) of RMS amplitude, with vertical error bars indicating the standard error of the mean (SEM). These error bars decrease over time, reflecting improved stability in the vibration prediction. The RSM LRR model shows better agreement with the experimental RMS, as it captures the broader amplitude variations observed in the measurements. In contrast, the EVM k-ω SST model predicts more consistent amplitudes but underestimates the experimental variability. Notably, the CMA for both URANS models converges after two seconds, suggesting that short 2 s simulations are sufficient to achieve reliable RMS amplitude estimates.

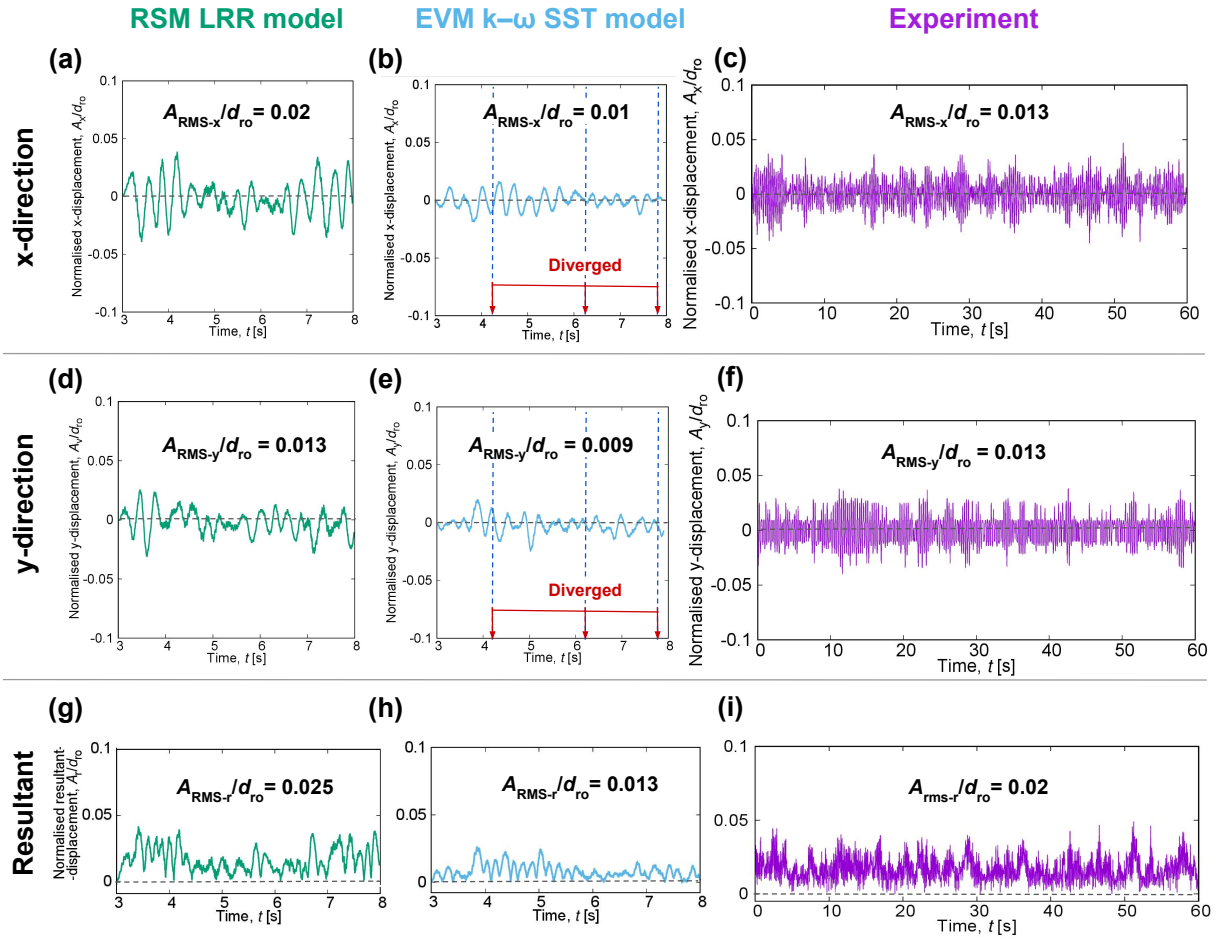

Figure 13. Displacement time series at an annulus Reynolds number of 35.1k for the UoM case, comparing the RSM LRR model (left column), the EVM k–ω SST model (middle column), and the experimental measurements (right column). The top row (**a**–**c**) shows the x-direction (A_x/d_{ro}), the middle row (**d**–**f**) shows the y-direction (A_y/d_{ro}), and the bottom row (**g**–**i**) shows the resultant displacement (A_r/d_{ro}). RMS-normalised amplitudes A_{RMS}/d_{ro} are annotated in each subplot. The EVM k–ω SST model results show divergence within the 5 s duration.

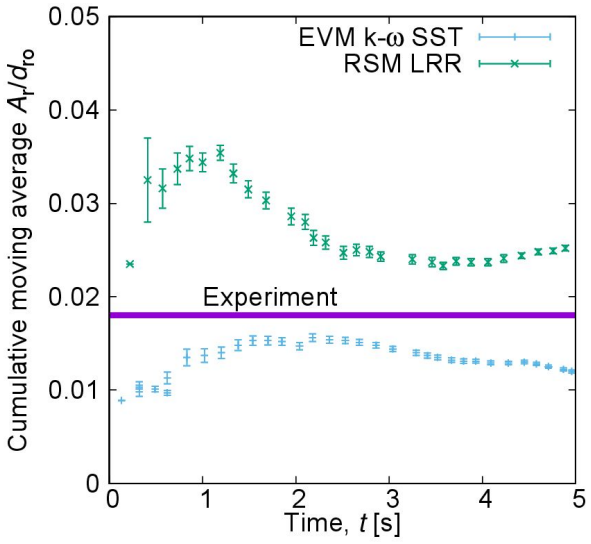

Figure 14. Cumulative moving average of the normalised resultant displacement (A_r/d_{ro}) for the RSM LRR and the EVM k-ω SST models at an annulus Reynolds number of 35.1k for the UoM case.

5.2. Varying Reynolds Numbers

5.2.1. Limitations for Upward Flow (Free-Fixed Configuration)

The axial-FIV simulations at varying Reynolds numbers are bounded by two key meshing limitations: a lower limit related to the correct application of logarithmic wall functions and an upper limit constrained by computationally feasible mesh refinement strategies.

For the lower limit, the fluid mesh was tailored to achieve a target near-wall non-dimensional distance (y*) of 30, ensuring compatibility with the logarithmic wall functions across varying Reynolds numbers. At the lowest annular Reynolds number tested (16.4 k), the reduced flow velocity would result in a lower y* if the same mesh used at Reynolds number of 35.1 k were applied. To address this, the near-wall cell size was increased, and two mesh variants were tested: a coarser mesh within the recommended y* range and a finer mesh below it, as shown in Figure 15a. As illustrated in Figure 15b, both meshes captured the unsteady flow near the free end, with the finer mesh showing sharper gradients. Nonetheless, the mechanical responses, RMS amplitude and first-mode frequency, remained within acceptable accuracy for both meshes.

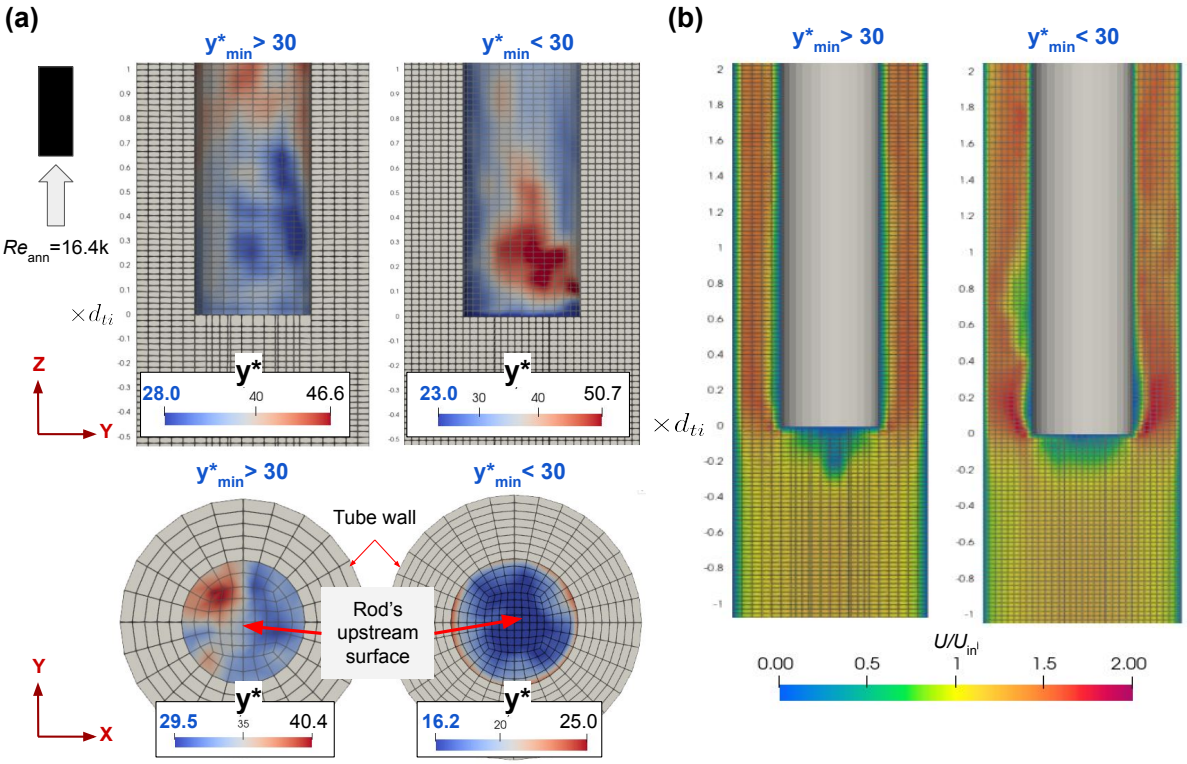

Figure 15. Contour plots of (**a**) instantaneous near-wall distance from the rod (y*) and (**b**) velocity (U/U_∞) at an annulus Reynolds number of 16.4 k using the RSM LRR model for the UoM case. For (**a**), the blue colour in the legend represents the minimum y*.

Figure 16 shows a clear increase in RMS vibration amplitude with rising annulus Reynolds number for both URANS models applied to the blunt end and only for the RSM LRR model applied to the curved end. The predictions align well with experimental data, remaining within the reported uncertainty range. The EVM k-ω SST model, however, demonstrated reduced numerical robustness, with repeated divergence across all tested Reynolds numbers, which increased its overall computational cost to roughly twice that of the RSM LRR model.

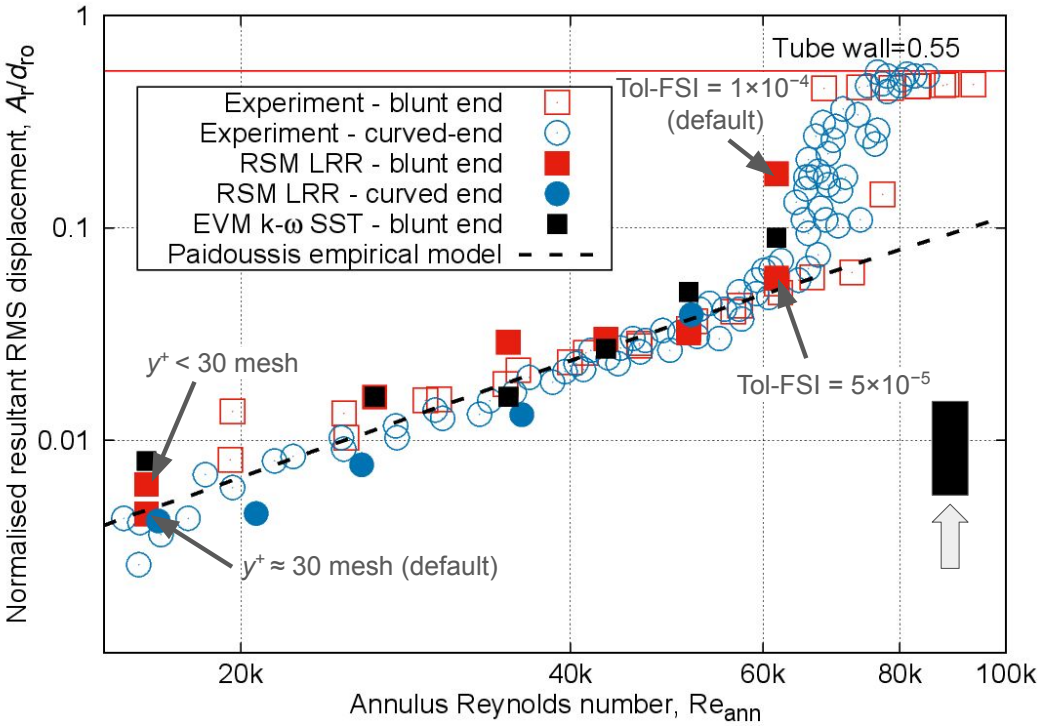

Figure 16. Normalised resultant RMS amplitude of vibration at varying annulus Reynolds numbers for the free-fixed configuration using the RSM LRR, the EVM k-ω SST models, and experiment measurements for the blunt end [21] and curved end [24] for the UoM case.

The simulations for the blunt end identified the onset of instability, marked by a significant jump in RMS amplitude, at 61.7 k, slightly earlier than the experimental threshold of 65–75 k. Applying a tighter FSI coupling tolerance at 61.7 k improved accuracy and kept the response within the small-amplitude random-vibration regime. Simulations at higher Reynolds numbers (>61.7 k) were not performed with either the baseline or the tighter FSI tolerance, as these cases require substantially greater computational resources. At such conditions, the increased wall shear stress raises the local y^+ for the same physical mesh spacing, hence resolving turbulence more accurately would require additional near-wall refinement, which lies beyond the scope of the present study.

At annulus Reynolds number of 61.7 k, the simulation diverged when the displacement reached approximately $0.07d_{ro}$, suggesting that large mesh deformations at high Reynolds numbers can destabilise the simulation, even with minor increases in mesh non-orthogonality. After divergence, the case was restarted from a statistically stable state. The rod then oscillated around a displaced equilibrium position (Figure 17b). Attempts to rerun the simulation from the beginning with lower solver relaxation factors failed due to divergence at large amplitudes. However, tightening the FSI coupling tolerance from 10^{-4} to 5×10^{-5} enabled the simulation to proceed beyond $0.068d_{ro}$, with divergence occurring only at the next vibration peak (Figure 17d). Restarting from a stable point a few hundred time steps earlier, the vibration resumed around the centreline until it reached computational limits.

For comparison, using the tighter FSI tolerance at a lower Reynolds number (51.3 k) did not significantly change the RMS amplitude (Figure 17a,c), indicating that the impact of FSI convergence criteria becomes more critical at higher Reynolds numbers. As such, the annulus Reynolds number of 61.7 k is identified as the upper simulation limit, beyond which tighter coupling tolerances are essential for stability and accuracy.

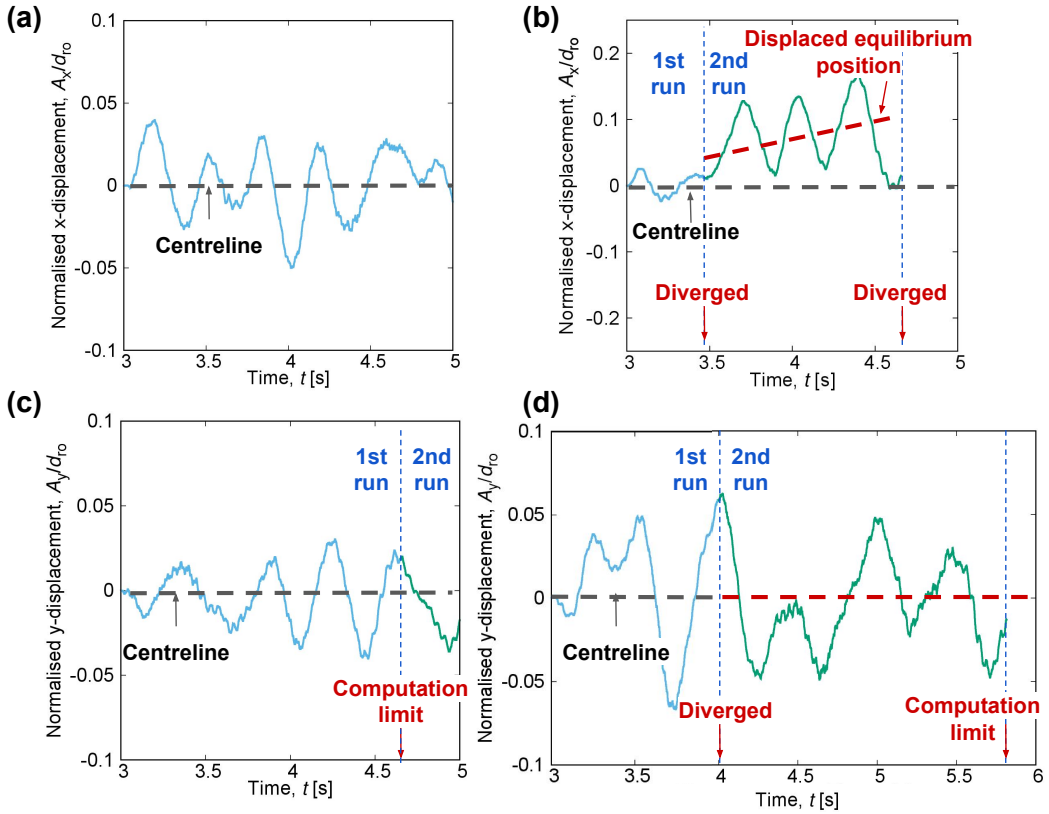

Figure 17. Displacement time series from simulations restarted at a stable point after initial divergence, using the RSM LRR model for the free–fixed configuration UoM case. Panels (**a**,**b**) show results with a default FSI tolerance of 1×10^{-4}, while panels (**c**,**d**) use a tighter tolerance of 5×10^{-5}. For both cases, the annulus Reynolds number is 51.3 k on the left (**a**,**c**) and 61.7 k on the right (**b**,**d**). The first and second simulation runs are indicated, with divergence and computation limits annotated.

5.2.2. Limitations for Downward Flow (Fixed–Free Configuration)

The URANS-FSI methodology was tested for downward flow (fixed–free configuration). Only the RSM LRR model successfully captured self-excited vibrations, while the EVM k-ω SST model produced small, non-physical deflections.

As shown in Figure 18, the RSM LRR model predicted acceptable RMS amplitude for the curved end. The simulation suggests an earlier onset of large-amplitude motion, with the transition occurring at 28.4 k compared with the experimental estimate of around 40 k. As this is based on only a few simulated points near the transition, the onset is taken as an approximate indication. For the blunt end, the model underpredicted vibration amplitude by two orders of magnitude. Experimental results show that end shape strongly influences the onset of instability: the curved end transitioned to flutter-like motion at lower Reynolds numbers, while the blunt end remained in small-amplitude vibration up to annulus Reynolds number of 90 k. These findings highlight a limitation of the URANS-FSI approach: its accuracy depends on end-shape stability, performing better for geometries that transition to instability motion at lower Reynolds numbers.

Furthermore, as observed in the free–fixed configuration, experimental measurements in the fixed–free configuration for both end shapes show a consistent increasing trend in RMS amplitude with Reynolds number, aligning with the empirical model. The curved end consistently overpredicts the empirical values by about a factor of two, while the blunt end shows closer agreement, although experimental values fall slightly below the empirical prediction as Reynolds number increases.

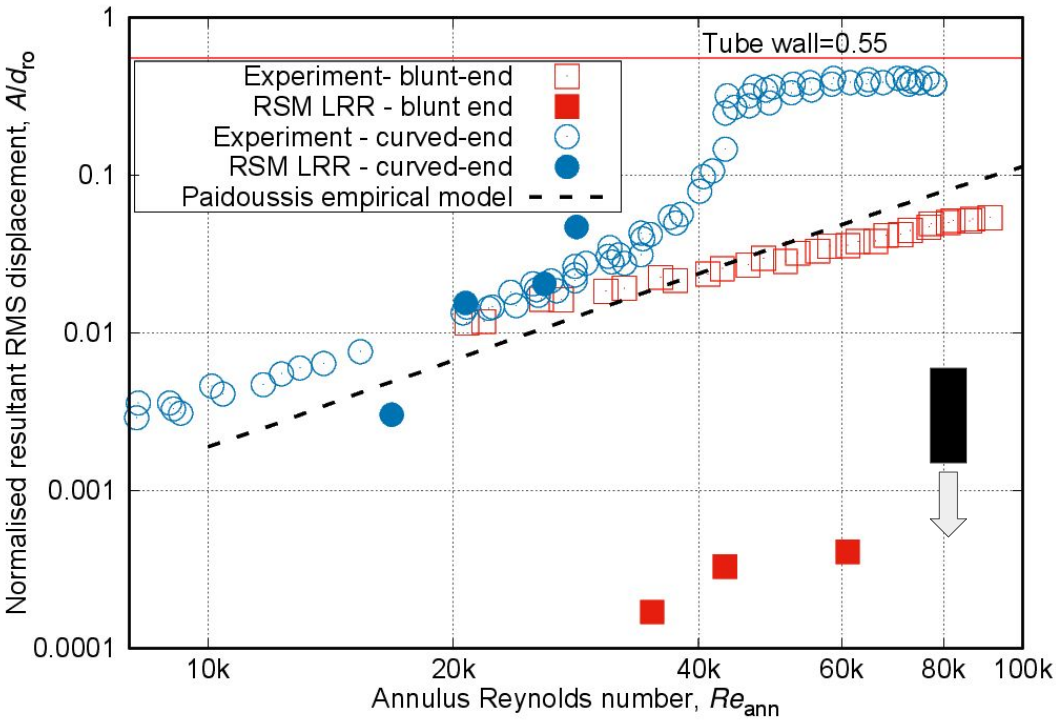

Figure 18. Normalised resultant RMS amplitude of vibration at varying annulus Reynolds numbers for the fixed-free configuration using the RSM LRR model and the experiment measurements for the blunt end [21] and curved end [24] for the UoM case.

6. Best-Practice Recommendations

Key recommendations are provided to enhance computational efficiency without compromising accuracy. In nuclear FIV analysis, accuracy is assessed using three primary parameters: first-mode frequency, damping ratio, and RMS amplitude, all extracted from the displacement time series. To ensure reliable prediction with minimal computational cost, distinct discretisation schemes, mesh strategies, and convergence criteria are proposed for each parameter, applicable to both RSM LRR and EVM k-ω SST models. Damping in axial flow is validated against the Vattenfall experiment, RMS amplitude from the self-excited axial-FIV University of Manchester experiment, while frequency is based on insights from both validation cases. A summary of the recommended best practices is presented in Table 7.

Table 7. Recommended numerical schemes, mesh requirement and convergence criteria for different FIV parameters.

Parameters	Numerical Schemes *		Mesh Requirement		Convergence Criteria	
	Momentum	Turbulent Variables	Solid	Fluid	Solid x-, y-, z-Coupling	FSI Coupling
Frequency	FOUS	FOUS	Fine mesh near fixed end	Coarse	Loose	Loose
Damping	CDS	FOUS		Fine mesh axially	Tight	Tight
RMS amplitude	CDS	FOUS		Fine mesh near free end	Moderate	Moderate

* Convection scheme for momentum and turbulence transport equations. Abbreviations: FOUS (first-order upwind scheme) and CDS (central differencing scheme).

To improve accuracy against experimental results, consider the following:

1. Where possible, avoid upwind schemes (both first and second order) for convection terms in the momentum equations, particularly in predicting damping and RMS amplitude.

2. Do not use first-order schemes or those with limiters that revert to first-order accuracy, such as TVD (OpenFOAM syntax "limitedLinear") or gradient limiters (OpenFOAM syntax "cellLimited" and "faceLimited").
3. Use second-order schemes for time discretisation, such as second-order Euler (OpenFOAM syntax "backward") or Crank–Nicolson (OpenFOAM syntax "CrankNicolson"), to better resolve unsteady behaviour near the free end.
4. Avoid the PIMPLE algorithm, which combines both PISO [34] and SIMPLE [53] algorithms, for pressure–velocity coupling, as it tends to smooth out transient flow features critical near the free end.
5. Refine the solid mesh near the fixed end to improve predictions of all frequency, damping ratio, and RMS amplitude.
6. Refine the fluid mesh near the free end to accurately resolve RMS amplitude of vibration.
7. For simulations involving curved ends, the RSM LRR model is recommended, as it consistently captures sufficient unsteadiness in the flow and therefore predicts the RMS amplitude more accurately than the EVM k-ω SST model.

To improve numerical stability and allow continuous simulation without divergence, consider the following:

1. Avoid higher-order convective schemes for turbulence equations, particularly with the EVM k-ω SST model, which may diverge due to large specific dissipation rate (ω) fluctuations.
2. Use a blended Crank–Nicolson scheme for time discretisation, gradually increasing the blending factor to reduce numerical dissipation without causing divergence.
3. For the EVM k-ω SST model, avoid using previous time-step information to minimise instability and divergence.
4. Maintain conformal circumferential mesh (Nc) at the FSI interface.
5. Ensure good mesh quality in the fluid domain by minimising non-orthogonality, skewness, and aspect ratio.
6. Use a finer axial mesh near the free end (dz-free) of the fluid domain to enable smooth restarts during interrupted simulations.
7. Avoid non-conformal meshes at the blunt-end rod's bottom surface to prevent instability at the FSI interface.
8. Tighten FSI coupling convergence criteria to avoid divergence, ensure smooth continuation after interrupted simulations, and prevent premature transition to flutter-like vibrations.

To enhance computational efficiency, which is critical for extending the displacement time series and improving result accuracy, consider the following:

1. Reduce the number of cells in the solid mesh by modelling the rod as hollow and concentrating mass in the cladding.
2. Increase axial mesh size away from the free end (dz-free), as pressure fluctuations near the fixed end have minimal influence on vibration.
3. Relax convergence criteria for the inter-component solid solver and FSI coupling where appropriate, as long as the validation parameters remain within acceptable accuracy.
4. If possible, use the RSM LRR model, as it is more stable in two-way FSI simulations and therefore more computationally efficient than the EVM k-ω SST model.
5. If the EVM k-ω SST model is required due to software limitations or integration with other physics, it can still provide reliable RMS amplitude predictions, especially when simulations are repeated to ensure consistency after interruptions.

7. Conclusions and Future Works

This study presents a validated URANS-FSI methodology for predicting key parameters of axial flow-induced vibration (axial FIV), which are frequencies, damping ratios, and RMS vibration amplitudes, with a focus on nuclear applications.

Building upon previous success in frequency prediction, this work emphasises on damping and RMS amplitude accuracy. Using the Vattenfall case, the methodology successfully captured damping in axial FIV. While the laminar model was able to predict damping even at high Reynolds numbers, it produced unphysical flow behaviour, whereas the URANS models provided more physically realistic solutions. Accurate damping prediction was found to require finer mesh resolution, particularly along the flow direction. Additionally, the IQN-ILS coupling algorithm outperformed the Gauss–Seidel method with Aitken relaxation in terms of convergence speed and computational efficiency.

Validation against the University of Manchester's self-excited axial-FIV experiments demonstrated that the URANS-FSI approach could accurately predict RMS amplitude across a range of Reynolds numbers, end shapes, and flow configurations.

As summarised in Table 8, the RSM LRR model proved to be the most reliable for capturing RMS amplitude, especially for curved-end rods in both free-fixed and fixed-free configurations and also for the blunt-end in the free-fixed case. In contrast, the EVM k-ω SST model only succeeded in the blunt-end free–fixed configuration and required longer simulation times with reduced stability.

Table 8. Capability of the URANS-FSI methodology in capturing RMS vibration amplitude for different flow configurations and end shapes in the self-excited axial-FIV simulations (UoM case).

Flow Configurations	End Shape	RSM LRR	EVM k-ω SST
Free–fixed	Blunt	Yes	Yes
	Curved	Yes	Several-order lower
Fixed–free	Blunt	Several-order lower	No self-sustain oscillation
	Curved	Yes	No self-sustain oscillation

For the fixed–free configuration, the URANS-FSI methodology was found to be sensitive to end-shape geometry: blunt ends suppressed the self-excited vibration amplitude by several orders of magnitude, while curved ends allowed accurate RMS amplitude prediction with the RSM LRR model but also exhibited large-amplitude flutter-like behaviour at lower Reynolds numbers. Furthermore, the empirical model proposed by Païdoussis [47] showed good agreement with both simulation and experimental results within the small-amplitude vibration region.

Limitations of the URANS-FSI method were observed at both ends of the Reynolds number spectrum. At lower Reynolds numbers, wall functions became invalid, though predictions of RMS amplitude remained accurate, suggesting that near-wall modelling may not be critical to predict the RMS amplitude. At higher Reynolds numbers, mesh deformation due to large vibration amplitudes affected simulation stability, particularly with ALE-based mesh strategies. This highlights the need to explore other meshing strategies such as multi-layer mesh techniques for improved mesh quality preservation. Moreover, the sensitivity to geometry implies that future work should investigate higher-order convection schemes to enhance the unsteady flow resolution required for accurate RMS predictions in two-way coupled FSI simulations.

Future work could extend this methodology by including simulations with heated water to better reflect reactor conditions. The influence of free-end geometry on axial FIV could also be examined, together with the effect of spacer-grid features such as springs, dimples, and mixing vanes on the inner tube wall. Multi-rod simulations with varied

pitch-to-diameter ratios could capture hydrodynamic coupling and vortex interactions, especially when combined with spacer-grid features.

In summary, this work provides a set of best-practice recommendations for predicting frequency, damping, and RMS amplitude in axial FIV using URANS-FSI. The methodology is computationally efficient and can be scaled to larger configurations, including full fuel-assembly and core-scale simulations. At these scales, it can help improve thermal-hydraulic performance while maintaining safe margins against large-amplitude instabilities. It provides a practical framework for predicting FIV and assessing the risk of fretting wear in reactor cores. The approach is also applicable to other nuclear components with similar slender tabular geometries, such as control rod guide tubes, steam generator tubes, and in-core instrumentation thimbles, and to other FIV scenarios involving high-stiffness structures in turbulent flows, such as those found in marine and aerospace systems.

Author Contributions: Conceptualisation, A.M.P., H.I. and A.C.; methodology, A.M.P. and W.M.; software, A.M.P. and W.M.; validation, A.M.P. and W.M.; formal analysis, A.M.P., W.M. and E.B.-D.; investigation, A.M.P. and W.M.; resources, A.C.; data curation, A.M.P. and W.M.; writing—original draft preparation, A.M.P.; writing—review and editing, A.M.P., E.B.-D., W.M., A.C. and H.I.; visualisation, A.M.P.; supervision, H.I. and A.C.; project administration, H.I.; funding acquisition, H.I. and A.C. All authors have read and agreed to the published version of the manuscript and agree to be accountable for all aspects of the work.

Funding: The authors gratefully acknowledge the financial support provided by Majlis Amanah Rakyat (MARA) from the Malaysian government. The experimental part of this work was performed within the European GO-VIKING Horizon project (Grant Agreement 101060826), which was funded by UK Research and Innovation (UKRI) under the UK Government's Horizon Europe funding guarantee (Grant Number 10058366). The support of EDF (France) and EDF-Energy (UK) is gratefully acknowledged.

Data Availability Statement: The original contributions presented in this study are included in the article. Further inquiries can be directed to the corresponding author.

Acknowledgments: The authors would like to thank the reviewers for their valuable comments and acknowledge the support of Research IT and the Computational Shared Facility at The University of Manchester.

Conflicts of Interest: This study received support from EDF (France) and EDF-Energy (UK), who funded the original construction of the experimental setup at the University of Manchester, UK. The funders were not involved in the design of the present study; in the collection, analysis, or interpretation of the data; in the development of the numerical methodology; in the writing of the manuscript; or in the decision to submit the article for publication.

Abbreviations

The following abbreviations are used in this manuscript:

CDS	Central difference scheme
CFD	Computational fluid dynamics
CMA	Cumulative moving average
dz-fixed	Axial mesh size near fixed end
dz-free	Axial mesh size near free end
dz-ratio	dz-fixed/dz-free
EVM	Eddy viscosity model
FIV	Flow-induced vibration
FSI	Fluid–structure interaction
GCI	Grid convergence index
IQN-ILS	Interface Quasi-Newton with Inverse Least Square approximation of Jacobian

LES	Large-eddy simulation
Nc	Number of intervals around the circumference
nCorr	Maximum number of correctors for solid inter-component coupling
nOuterCorr	Maximum number of iterations for the FSI coupling
NPP	Nuclear power plant
Nr-ann	Number of intervals in the annulus gap
PISO	Pressure-Implicit with Splitting of Operators pressure–velocity coupling
PWR	Pressurised Water Reactor
reuseCoupling	Number of time step information used for FSI coupling
RMS	Root-mean square
RSM	Reynolds stresses model
Sol-FSI	Convergence tolerance for the FSI coupling
Sol-S	Convergence tolerance for the solid solver
UoM	The University of Manchester, United Kingdom
URANS	Unsteady Reynolds-Averaged Navier–Stokes equations
URANS-FSI	A numerical framework combining URANS modelling and two-way FSI coupling

References

1. International Atomic Energy Agency. *Review of Fuel Failures in Water Cooled Reactors*; IAEA: Vienna, Austria, 2010; ISBN 978-92-0-102610-1. Available online: https://www.iaea.org/publications/8259/review-of-fuel-failures-in-water-cooled-reactors (accessed on 17 December 2025).
2. International Atomic Energy Agency. *Review of Fuel Failures in Water Cooled Reactors (2006–2015): An Update of IAEA Nuclear Energy Series No. NF-T-2.1*; IAEA: Vienna, Austria, 2019; ISBN 978-92-0-104319-1. Available online: https://www.iaea.org/publications/13383/review-of-fuel-failures-in-water-cooled-reactors-2006-2015 (accessed on 17 December 2025).
3. Jiang, N.; Min, G.; Fang, Z.; Qi, H. Investigation on vibration response characteristics and influencing factors of the fuel rods of EPR. *Front. Energy Res.* **2022**, 10, 990525. [CrossRef]
4. Casabianca, J. *The Inspector General's Report on Nuclear Safety and Radiation Protection*; EDF Energy: Paris, France, 2023.
5. Benhamadouche, S.; Moussou, P.; Le Maitre, C. CFD estimation of the flow-induced vibrations of a fuel rod downstream a mixing grid. In *Proceedings of the ASME Pressure Vessels and Piping Division Conference (PVP), Prague, Czech Republic, 26–30 July 2009*; ASME: New York, NY, USA, 2009; Volume 4, pp. 489–497. [CrossRef]
6. Zhang, X.; Yu, S.D. Large eddy simulation of turbulent flow surrounding two simulated CANDU fuel bundles. *Nucl. Eng. Des.* **2011**, 241, 3553–3572. [CrossRef]
7. Liu, Z.G.; Liu, Y.; Lu, J. Fluid-structure interaction of single flexible cylinder in axial flow. *Comput. Fluids* **2012**, 56, 143–151. [CrossRef]
8. Liu, Z.G.; Liu, Y.; Lu, J. Numerical simulation of the fluid-structure interaction for an elastic cylinder subjected to tubular fluid flow. *Comput. Fluids* **2012**, 68, 192–202. [CrossRef]
9. De Ridder, J.; Degroote, J.; Van Tichelen, K.; Schuurmans, P.; Vierendeels, J. Predicting turbulence-induced vibration in axial annular flow by means of large-eddy simulations. *J. Fluids Struct.* **2015**, 61, 115–131. [CrossRef]
10. Nazari, T.; Rabiee, A.; Kazeminejad, H. Two-way fluid-structure interaction simulation for steady-state vibration of a slender rod using URANS and LES turbulence models. *Nucl. Eng. Technol.* **2019**, 51, 573–578. [CrossRef]
11. Norddine, T.; Benhamadouche, S. Wall-Resolved LES and URANS Simulations of an Axial Flow on a Cantilevered Rod at a Moderate Reynolds Number. In *Proceedings of the 20th International Topical Meeting on Nuclear Reactor Thermal Hydraulics (NURETH-20), Washington, DC, USA, 20–25 August 2023*; American Nuclear Society: La Grange Park, IL, USA, 2023; pp. 4632–4645. [CrossRef]
12. Elmahdi, A.M.; Lu, R.; Conner, M.E.; Karoutas, Z.; Baglietto, E. Flow induced vibration forces on a fuel rod by LES CFD analysis. In Proceedings of the 14th International Topical Meeting on Nuclear Reactor Thermal Hydraulics (NURETH-14), Toronto, ON, Canada, 25–30 September 2011; pp. 1–6.
13. Bakosi, J.; Christon, M.A.; Lowrie, R.B.; Pritchett-Sheats, L.A.; Nourgaliev, R.R. Large-eddy simulations of turbulent flow for grid-to-rod fretting in nuclear reactors. *Nucl. Eng. Des.* **2013**, 262, 544–561. [CrossRef]
14. Papadimitriou, V. HPC FSI Simulation of a Rod Subjected to Axial Turbulent Flow: Calculations for Nuclear Power Applications. Master's Thesis, KTH Royal Institute of Technology, Stockholm, Sweden, 2016. Available online: https://energiforskmedia.blob.core.windows.net/media/19405/hpc-fsi-simulation-of-a-rod-subjected-to-axial-turbulent-flow-energiforskrapport-2016-269.pdf (accessed on 17 December 2025).

15. Amirian, R.; Zarepoor, G.R.; Talebi, M. Numerical simulation and validation of flow-induced vibration of the specific rod under elastic supports using one-way fluid-solid interaction. *J. Appl. Fluid Mech.* **2023**, 16, 1044–1056. [CrossRef]
16. Lillberg, E.; Angele, K.; Lundqvist, G.; Edh, N. Tailored experiments for validation of CFD with FSI for nuclear applications. In *Proceedings of the 16th International Topical Meeting on Nuclear Reactor Thermal Hydraulics (NURETH-16), Chicago, IL, USA, 30 August–4 September 2015*; American Nuclear Society: La Grange Park, IL, USA, 2015. Available online: http://glc.ans.org/nureth-16/data/papers/14093.pdf (accessed on 17 December 2025).
17. De Pauw, B.; Weijtjens, W.; Vanlanduit, S.; Van Tichelen, K.; Berghmans, F. Operational modal analysis of flow-induced vibration of nuclear fuel rods in a turbulent axial flow. *Nucl. Eng. Des.* **2015**, 284, 19–26. [CrossRef]
18. Chen, S.; Wambsganss, M.W. Parallel-flow-induced vibration of fuel rods. *Nucl. Eng. Des.* **1972**, 18, 253–278. [CrossRef]
19. Cioncolini, A.; Silva-Leon, J.; Cooper, D.; Quinn, M.K.; Iacovides, H. Axial-flow-induced vibration experiments on cantilevered rods for nuclear reactor applications. *Nucl. Eng. Des.* **2018**, 338, 102–118. [CrossRef]
20. Cioncolini, A.; Zhang, S.; Nabawy, M.R.A.; Li, H.; Cooper, D.; Iacovides, H. Experiments on axial-flow-induced vibration of a free-clamped / clamped-free rod for light-water nuclear reactor applications. *Ann. Nucl. Energy* **2023**, 190, 109900. [CrossRef]
21. Muhamad Pauzi, A.; Iacovides, H.; Cioncolini, A.; Li, H.; Nabawy, M.R.A. Application of URANS simulation and experimental validation of axial flow-induced vibrations on a blunt-end cantilever rod for nuclear applications. *Arab. J. Sci. Eng.* **2025**, 50, 3435–3455. [CrossRef]
22. De Santis, D.; Shams, A. Numerical modeling of flow induced vibration of nuclear fuel rods. *Nucl. Eng. Des.* **2017**, 320, 44–56. [CrossRef]
23. Salachna, J.; Cioncolini, A.; Iacovides, H. Benchmark simulation of the flow-induced vibrations for nuclear applications. *Ann. Nucl. Energy* **2023**, 180, 109425. [CrossRef]
24. Mao, W.; Iacovides, H.; Cioncolini, A.; Li, H.; Nabawy, M.R.A. A validated numerical methodology for flow-induced vibration of a semi-spherical end cantilever rod in axial flow. *Phys. Fluids* **2024**, 36, 075155. [CrossRef]
25. ter Hofstede, E.; Kottapalli, S.; Shams, A. Numerical prediction of flow induced vibrations in nuclear reactor applications. *Nucl. Eng. Des.* **2017**, 319, 81–90. [CrossRef]
26. De Santis, D.; Shams, A. An advanced numerical framework for the simulation of flow induced vibration for nuclear applications. *Ann. Nucl. Energy* **2019**, 130, 218–231. [CrossRef]
27. De Ridder, J.; Degroote, J.; Van Tichelen, K.; Schuurmans, P.; Vierendeels, J. Modal characteristics of a flexible cylinder in turbulent axial flow from numerical simulations. *J. Fluids Struct.* **2013**, 43, 110–123. [CrossRef]
28. Zwijsen, K.; Tajfirooz, S.; Roelofs, F.; Papukchiev, A.; Edh, N.; Lillberg, E. Modeling of axial flow-induced vibrations of a BWR instrumentation guide tube experiment. *Nucl. Eng. Des.* **2024**, 427, 113444. [CrossRef]
29. Menter, F.R. Two-equation eddy-viscosity turbulence models for engineering applications. *AIAA J.* **1994**, 32, 1598–1605. [CrossRef]
30. Papukchiev, A.; Pandazis, P.; Hristov, H.; Scheuerer, M. Validation of Coupled CFD–CSM Methods for Vibration Phenomena in Nuclear Reactor Cores. In *Advances in Critical Flow Dynamics Involving Moving/Deformable Structures with Design Applications*; Braza, M., Hourigan, K., Triantafyllou, M., Eds.; Notes on Numerical Fluid Mechanics and Multidisciplinary Design; Springer: Cham, Switzerland, 2021; Volume 147, pp. 55–69. [CrossRef]
31. Kottapalli, S.; Shams, A.; Zuijlen, A.H.; Pourquie, M.J.B.M. Numerical investigation of an advanced U-RANS based pressure fluctuation model to simulate non-linear vibrations of nuclear fuel rods due to turbulent parallel-flow. *Ann. Nucl. Energy* **2019**, 128, 115–126. [CrossRef]
32. Muhamad Pauzi, A.; Iacovides, H.; Cioncolini, A. Pragmatic modelling of axial flow-induced vibration (FIV) for nuclear fuel rods. *IOP Conf. Ser. Mater. Sci. Eng.* **2023**, 1285, 012001. [CrossRef]
33. Cardiff, P.; Karač, A.; De Jaeger, P.; Jasak, H.; Nagy, J.; Ivanković, A.; Tuković, Ž. An open-source finite volume toolbox for solid mechanics and fluid-solid interaction simulations. *arXiv* **2018**, arXiv:1808.10736. [CrossRef]
34. Issa, R.I. Solution of the Implicitly Discretised Fluid Flow Equations by Operator-Splitting. *J. Comput. Phys.* **1986**, 62, 40–65. [CrossRef]
35. Tuković, Ž.; Perić, M.; Jasak, H. Consistent Second-Order Time-Accurate Non-Iterative PISO-Algorithm. *Comput. Fluids* **2018**, 166, 78–85. [CrossRef]
36. Launder, B.E.; Reece, G.J.; Rodi, W. Progress in the development of a Reynolds-stress turbulence closure. *J. Fluid Mech.* **1975**, 68, 537–566. [CrossRef]
37. Launder, B.E.; Sharma, B.I. Application of the energy-dissipation model of turbulence to the calculation of flow near a spinning disc. *Lett. Heat Mass Transf.* **1974**, 1, 131–137. [CrossRef]
38. Jasak, H.; Weller, H.G. Application of the finite volume method and unstructured meshes to linear elasticity. *Int. J. Numer. Methods Eng.* **2000**, 48, 267–287. [CrossRef]
39. Tuković, Ž.; Jasak, H.; Karač, A.; Cardiff, P.; Ivanković, A. OpenFOAM finite volume solver for fluid-solid interaction. *Trans. Famena* **2018**, *42*, 1–31. [CrossRef]

40. Cardiff, P. Development of the Finite Volume Method for Hip Joint Stress Analysis. Ph.D. Thesis, University College Dublin, Dublin, Ireland, 2012. Available online: http://hdl.handle.net/10197/7919 (accessed on 17 December 2025).
41. Girfoglio, M.; Quaini, A.; Rozza, G. Fluid-Structure Interaction Simulations with a LES Filtering Approach in solids4Foam. *arXiv* **2021**, arXiv:2102.08011v2. [CrossRef]
42. Degroote, J. Partitioned Simulation of Fluid-Structure Interaction: Coupling Black-Box Solvers with Quasi-Newton Techniques. *Arch. Comput. Methods Eng.* **2013**, 20, 185–238. [CrossRef]
43. Burgreen, D.; Byrnes, J.J.; Benforado, D.M. Vibration of Rods Induced by Water in Parallel Flow. *Trans. ASME* **1958**, 80, 991–1003. [CrossRef]
44. Quinn, E.P. *Vibration of SEFOR Fuel Rods in Parallel Flow*; Report No. GEAP-4059; General Electric Co., Atomic Power Equipment Dept.: San Jose, CA, USA, 1962. Available online: https://www.osti.gov/biblio/4748757 (accessed on 17 December 2025).
45. Societe Grenobloise d'Etude et d'Applications Hydrauliques (SOGREAH). *Research into Vibrations and Load Losses in Tabular Clusters*; Technical Report; SOGREAH: Grenoble, France, 1962. Available online: https://www.osti.gov/biblio/4793818 (accessed on 17 December 2025).
46. Roström, K.G.; Andersson, N. *Boiler Element for Marviken: Vibration Tests with One Rod*; Arbetsrapport RRL-724; AB Atomenergi: Stockholm, Sweden, 1964.
47. Païdoussis, M.P. Dynamics of Flexible Slender Cylinders in Axial Flow. Part 2. Experiments. *J. Fluid Mech.* **1966**, 26, 737–751. [CrossRef]
48. Païdoussis, M.P. *Fluid–Structure Interactions: Slender Structures and Axial Flow*, 2nd ed.; Academic Press, Elsevier: Oxford, UK, 2016; Volume 2. [CrossRef]
49. Païdoussis, M.P.; Sharp, F.L. *An Experimental Study of the Vibration of Flexible Cylinders Induced by Nominally Axial Flow*; Technical Report CRNL-76; Atomic Energy of Canada Limited: Chalk River, ON, Canada, 1967.
50. *ASME V&V 20-2009*; Standard for Verification and Validation in Computational Fluid Dynamics and Heat Transfer. American Society of Mechanical Engineers: New York, NY, USA, 2009.
51. Degroote, J.; Haelterman, R.; Annerel, S.; Swillens, A.; Segers, P.; Vierendeels, J. An interface quasi-Newton algorithm for partitioned simulation of fluid-structure interaction. In Proceedings of the International Workshop on Fluid–Structure Interaction: Theory, Numerics and Applications, Herrsching am Ammersee, Germany, 29 September–1 October 2008; p. 55.
52. Muhamad Pauzi, A. URANS–FSI Case Files for Axial Flow-Induced Vibration of a Cantilever Rod for Nuclear Application [Dataset]. Zenodo, 2025. [CrossRef]
53. Patankar, S.V.; Spalding, D.B. A calculation procedure for heat, mass and momentum transfer in three-dimensional parabolic flows. *Int. J. Heat Mass Transf.* **1972**, 15, 1787–1806. [CrossRef]